

Norwegian University of Life Sciences
Faculty of Environmental Science and
Technology
Department of Mathematical Sciences and
Technology

Master Thesis 2015
30 credits

Understanding Resonant Structures of Coupled Disks for Light Management in Photovoltaics

Maren Anna Brandsrud

Acknowledgements

This thesis is the fulfillment of my Master's degree at the Norwegian University of Life Sciences (NMBU).

I would like to thank my supervisors, Prof. Achim Kohler and Dr. Rozalia Lukacs for guidance and advice.

I would also like to thank my friends for great years at NMBU. These years would not have been the same without you! Thanks to Ingrid and Hanne for patience, encouragements and several lunches and dinners during the last months.

Finally, yet importantly, I would like to thank Ole-Johan, Inger Johanne and my parents for support and encouragements.

Ås, December 15, 2015

Maren Anna Brandsrud

Abstract

Thin film solar cells offer a reduced material usage at the expense of lower efficiency. Effective light management in nanostructures can contribute to an increasing efficiency and absorption of energy in the devices. Recently, it could be shown that nanoimprints on thin film solar cells increase the efficiency of thin-film solar cells considerably, while the rationale for the increased efficiency is only partially understood. The aim of this thesis was to investigate to what extent a coupling of spheres explains the absorption enhancement by spherical nanoimprints. For this purpose different systems of two dimensional disks were investigated as a model system. Both the ray dynamics and the wave dynamics in these systems were investigated. For the ray dynamics, a ray model with a deterministic selection rule was implemented. The wave dynamics was investigated by a plane-wave scatter code based on the Lippmann-Schwinger equation. The ray model with a deterministic selection rule revealed a chaotic phase space for a two-disk system with low refractive indices. For high refractive indices, a phase space with strange attractors was observed. An evaluation of the plane-wave scattering code showed that it is stable. It allowed the investigation of coupled modes in various multiple-disk systems with equally and differently sized disks. Several of the coupled modes could be directly related to strange attractors. For this purpose a quantization rule was established which connected the strange attractor rays directly to coupled modes. This shows that the ray dynamics can potentially be used to understand and optimized architectures of nanoimprints. It was further observed that when the ray dynamics changed from a chaotic phase space to a phase space with strange attractors, the corresponding resonances in the wave mechanics were considerably enhanced. An exploration of the ray dynamics for the enhancement of architectures of nanoimprints will require a deeper investigation.

Sammendrag

Tynnfilm solceller fører til et lavere materialforbruk, dette på kostnad av effektiviteten. Effektiv lysledning i nanostrukturer kan føre til økt effektivitet og energiabsorpsjon i solcellene. Det kan vises at sfæriske nanoavtrykk øker effektiviteten til tynnfilm solceller vesentlig, men årsaken til den økte effektiviteten er kun delvis forstått. Hensikten med denne oppgaven var å undersøke i hvilken grad koblingen mellom sfærene kan forklare økningen i absorpsjon grunnet sfæriske nanoavtrykk. Derfor er flere todimensjonale disksystemer brukt som modeller i undersøkelsene. Både stråle- og bølgedynamikk har blitt undersøkt for disse modellene. For stråledynamikken ble en bølgemodell med en deterministisk utvalgsregel implementert. Bølgedynamikken ble undersøkt med en kode som viser spredning av en planbølge, koden er basert på Lippmann-Schwingers likning. Strålingsmodellen med deterministisk utvalgsregel avslørte et kaotisk faserom for lave brytningsindekser. For høye brytningsindekser hadde faserommet rare attraktorer. Koden for spredning av planbølgen viser seg å være stabil. Den tillater undersøkelser av koblingen mellom systemer som består av flere disker med lik og ulik størrelse. Flere av koblingene kan direkte bli knyttet til rare attraktorer. En kvantiseringsregel ble derfor etablert, dette for å knytte attraktorene direkte til koblingene. Dette betyr at strålingsmodellen potensielt kan brukes til å forstå og optimalisere arkitekturen av nanoavtrykket. Det var videre observert at når strålingsdynamikken endret fra et kaotisk faserom til et faserom med rare attraktorer, ble de korresponderende resonansene i bølgedynamikken vesentlig økt. En undersøkelse av strålingsdynamikken for forbedringen av arkitekturen til nanoavtrykk vil kreve videre undersøkelser.

Contents

Chapter 1	Introduction	1
Chapter 2	Classical ray dynamics in two-dimensional systems	4
2.1	Ray dynamics in two-disk systems.....	4
2.1.1	Ray model with selection rule for the two-disk system.....	5
2.1.2	Poincaré Surface of Section for the two-disk system	7
2.2	Ray dynamics in arrays of disks	18
Chapter 3	Plane wave scattering in disk systems	20
3.1	Resonances and whispering gallery modes in highly scattering systems.....	20
3.2	Plane-wave scattering algorithm	23
3.3	Plane-wave scattering in two-disk systems.....	26
3.4	Plane-wave scattering in three-disk system.....	39
3.5	Plane-wave scattering in two-disk system with differently sized disks	41
3.6	Plane-wave scattering in one-disk systems	43
3.7	Effect of the direction of the incoming plane wave on resonances in the two-disk system	48
Chapter 4	Discussion	53
Chapter 5	Conclusion and outlook.....	57
Bibliography	59
Appendix	62

Chapter 1

Introduction

The amount of solar energy that every year hits the atmosphere of the Earth is equal to 5,4 millions EJ. While the atmosphere reflects 30 % of this energy; the rest is available for use on Earth⁴. Photovoltaic solar cells convert the energy of the sunlight into green electrical energy. Since decades, the crystalline silicon solar cells with efficiency higher than 20 % have dominated the market. Their thickness ranges between 150 and 300 μm . The increasing need for clean energy has led to an enforced effort in the development of photovoltaic devices to reduce materials usage and production costs. Thin film solar cells offer a potential technology that provides a step toward solving these challenges²⁰.

Traditionally, light trapping has been a method for enhancing short-circuit current by enhancing the photo carrier generation of solar cells. This technology is becoming more and more effective. The use of light management has led to an increasing efficiency of light-trapping strategies and thus increased the efficiency of thin film solar cells²⁰. Thin film solar cells offer a reduced material usage and lower production cost at the expense of lower efficiency⁷. Today, several methods of light trapping exist. Light trapping by imprinting a texture on the light absorbing material that enhances the absorption properties of the material has been identified as a potential solution⁸. Nanostructures are used in solar cells to enhance the light absorption²⁰. Since different nanostructures architectures reveal different light scattering and absorption properties, it is important to understand how different parameters effect the efficiency of the structures²⁰. It has for example been shown that spherical nanoshells in contact with a photovoltaic device absorb significantly more than a flat film solar cell^{7, 31}. These spherical structures also accept light from larger angles of incidence⁷. Recently, Grandidier et al.⁷ presented experimental results for a-Si (amorphous silicon) solar cell with closely packed dielectric resonant nanospheres on the top of the device. They showed that an increased spectral current density could be obtained for the whole wavelength range when dielectric

resonance nanospheres were added to the top of the device. For specific wavelengths the increase was up to 12 %. This clearly shows the potential of nanostructures in energy converting materials⁷. The efficiencies of the nanostructures were described by resonant Mie electric and magnetic modes of single spheres. These resonant modes correspond to whispering gallery modes inside the single spheres of nanostructures⁷. While the effect of Mie resonances of single spheres on the absorption properties has been discussed in literature¹⁰, the effect of coupling of spheres and the contribution of the coupling to an enhancement of the absorption properties has not been given the same attention yet. The hypothesis of this thesis is that the whispering gallery modes alone do *not* explain the total enhancement achieved in absorption. It is hypothesized that a coupling of the near field between the nanostructures may contribute significantly to the enhancement. Thus, the main aim of this thesis was to investigate resonant structures of coupled spheres. Due to the complexity of the problem in three dimensions, we restricted our self to the investigation of two-dimensional disk systems.

For coupled modes, analytic solutions of Maxwell equations for coupled nanostructures do not exist. To evaluate such structures the finite difference time domain (FDTD) technique has been used. Since this simulation technique does not provide a deeper inside into how the geometrical arrangement, size of spheres and the materials can influence the light management and since it is numerically difficult and time-consuming it was not considered as a possible approach in this thesis.

Another approach for investigating nanostructured light trapping, is an approach introduced by Ryu and Hentschel²⁵ to study the coupling of optical microdisks based on a classical ray dynamics. They introduced a deterministic selection rule for coupled optical microdisks for a two-disk system. Ray dynamics in ray-splitting systems and its implications for the corresponding quantum systems have been studied extensively in the field of quantum chaos^{9, 13-17, 26}. The advantage of the approach is that by the help of classical periodic rays, quantum phenomena could be elucidated and a deeper understanding of the system could be obtained. Chapter 2 of this thesis presents an investigation of the classical ray dynamics of a two-disk system and for more than two disks. For the investigation of the classical ray dynamics, the deterministic selection rule introduced by Ryu and Hentschel²⁵ is used.

In order to investigate absorption resonances in the corresponding wave system a new scattering code for multi-disk systems was evaluated. The code is based on the Lippmann-Schwinger equation where the incoming wave is a plane wave. The theory for the scattering algorithm and simulation results are presented in chapter 3. The stability and versatility of the program is discussed and evaluated.

In the appendix, the codes for the classical two-disk system with a deterministic selection rule are presented. The scattering code for multi-disk systems is also given in the appendix.

Chapter 2

Classical ray dynamics in two-dimensional systems

2.1 Ray dynamics in two-disk systems

According to Fermat's principle, a light beam travelling through a medium with a constant refractive index will follow a straight line²². When the ray strikes a boundary that is separating two media with different refractive indices, the light is either reflected or transmitted²². This situation is illustrated in Fig. 2.1. The transmitted ray is subjected to a change in direction. This change in direction depends on the angle of incidence and the ratio between the refractive indices of the two media. This phenomenon is called *refraction*²².

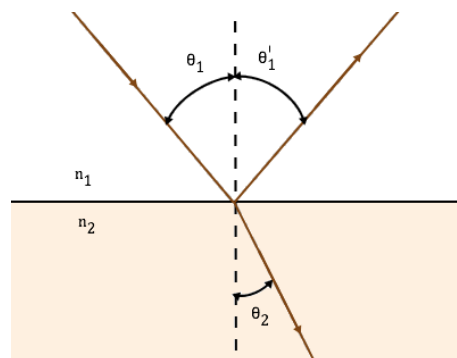


Figure 2.1 A ray incident on the interface of two media. The angle of incidence is denoted by θ_i . This angle θ_i is equal to the angle of reflection θ'_i . The transmitted ray is refracted leading to a change in direction. The angle of refraction is denoted by an angle θ_r . It depends on the angle of incidence and ratio between the refractive indices of the media. The refractive indices of the two media are denoted by n_1 and n_2 are.

The angle of incidence θ_1 and the angle of refraction θ_2 (see Fig. 2.1) are related by Snell's law of refraction²²

$$n_1 \sin \theta_1 = n_2 \sin \theta_2 \quad (2-1)$$

where n_1 is the refractive index of the medium in which the incident ray moves and n_2 is the refractive index of the medium in which the refracted ray moves. *Total internal reflections* can appear when an incoming ray is coming from a medium with high refractive index to a medium with lower refractive index, i.e. $n_1 > n_2$. In this case $\theta_2 > \theta_1$, meaning that for an angle $\theta_1 < 90^\circ$ and angle $\theta_2 = 90^\circ$ will be achieved. When θ_1 reaches $\theta_1 = 90^\circ$ in Eq. 2-1, we call the corresponding angle θ_1 critical angle θ_c . If the incoming ray has an angle of incidence larger than the critical angle of total internal reflection, no light is transmitted²². When a ray has an angle of incidence equal to the critical angle, the light ray continues along the surface of incidence, i.e. the angle of refraction would then be $\frac{\pi}{2}$ radians.

2.1.1 Ray model with selection rule for the two-disk system

In the following, we introduce the two-disk system that will be studied in this thesis. The two-disk system is shown in Fig. 2.2. The two disks have a distance d . The radii of the left and right disk are r_1 and r_2 , respectively. In almost all cases in this thesis the radii r_1 and r_2 are identical and equal. If different radii are used, this is explicitly stated in the text. The refractive indices n_1 and n_2 are the refractive indices of the surrounding medium and the disks, respectively. The arc length along the boundary at the left disk is indicated by s . By $s = 0$ we denote the point at the left disk where the array that indicates increasing s starts.

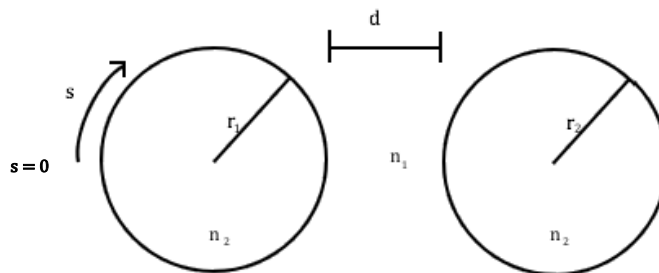


Figure 2.2 The two-disk system consists of two equal disks. The radii of the left and right disk are denoted by r_1 and r_2 , respectively, d is the shortest distance between the boundaries of the disks. s indicates the arc length along the disk boundary. The refractive indices of the surrounding medium and the disks are denoted by n_1 and n_2 , respectively.

According Snell's law of refraction (Eq. 2-1), the ratio of the refractive indices is determining the direction of the ray after transmission. In this thesis the refractive index, n , denotes the refractive ratio $n = \frac{n_2}{n_1}$, i.e. the ratio of the refractive index of the disks and the refractive index of the surrounding medium.

In order to describe the ray dynamics of the two-disk system, we will follow the ray dynamics introduced by Ryu and Hentschel²⁵. The ray dynamics of Ryu and Hentschel²⁵ includes a deterministic selection rule in order to force the rays to continue inside the disks. Each time a ray hits the ray-splitting boundary from the inside of one of the disks, the ray may be reflected or transmitted. Previously, ray-splitting situations have been handled with probabilistic rules^{2, 5, 14}, i.e. based on a probability it is decided, if the ray is reflected or transmitted. If the ray is transmitted, the chance to hit the neighboring disk is low and all rays may leave the system within short time. In order to keep all rays permanently in the two-disk system, Ryu and Hentschel²⁵ defined a deterministic selection rule. The deterministic ray splitting rule works as follows: Rays are transmitted from the inside to the outside of a disk only if the disk can hit the other disk and thus stay in the system. A consequence of this selection rule is that a ray cannot escape from the system.

For the ray model, the ray dynamics does not change if the ratio between the radius of the disks and the distance between disks is kept constant. Thus, for the description of the ray dynamics, the ratio between these variables is given.

In order to simulate the ray dynamics for the two-disk system the deterministic ray dynamics of Ryu and Hentschel²⁵ was implemented in Matlab. The corresponding Matlab script, *plot_ray.m*²⁴, can be found in the appendix. The deterministic ray dynamics is illustrated in Fig. 2.3. The ray starts from top of the left disk, with an angle equal 17.2 degrees to the left of the normal on the surface of the disk. The refractive index ratio is $n = 1.9$ for the system. The distance between the disks is equal to the radius.

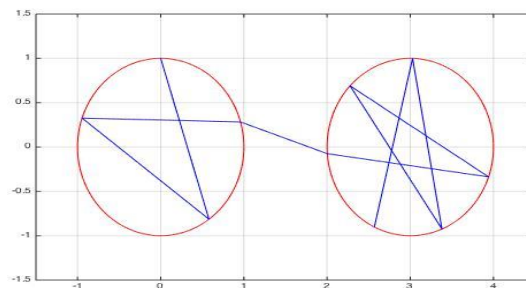


Figure 2.3 The start point of the ray is at the top of the left disk with an angle of 17.2 degrees to left of the normal of the surface. The ratio between the refractive indices is $n = 1.9$. The distance between the disks is equal to the radius, i.e. $d = r$.

The coordinate system that is used in this thesis for the classical disk system is the Birkhoff coordinate system, which was defined by Berry¹. The Birkhoff coordinate system consists of two coordinates. The first coordinate is s , which denotes the arc length, as indicated in Fig. 2.2. In this thesis s is given as a fraction of the total length of the upper part of the left disk

$$s = \frac{\text{arc length of the upper half disk}}{\pi * r} \quad (2-2)$$

where r is the radius of the disk and the arc length of the upper half disk is increasing in the direction of the array indicated in Fig. 2.2. Thus, s , is a number between 0 and 1. The other coordinate is p , which terms the momentum

$$p = \sin(\theta) \quad (2-3)$$

where θ is the angel of incidence measured to the left of the normal on the surface of the disk. The momentum p is thus a number between -1 and 1. To allow a ray to escape from the inside to the outside of a disk, the angle θ has to be equal or smaller than the critical angle. If the momentum $p > 0$, we say that the ray circulates clockwise, while when $p < 0$ we say that the ray circulates counterclockwise

2.1.2 Poincaré Surface of Section for the two-disk system

By studying the phase space of the ray model in terms of the Poincaré surface of section (PSOS) of the upper half of the left disk, the stabile and chaotic regions of the phase space can be identified. We following the definition of Ryu and Hentschel²⁵, where the PSOS is obtained by plotting s (Eq. 2-2) against p (Eq. 2-3). This is done for the transmissions and reflections at the boundary of the upper half of the left disk in a given interval. Because of symmetry, it is sufficient to evaluate the PSOS only in the upper half of the left disk.

The PSOS is obtained after a number of the transmissions and reflections of the ray. This is done because a random ray does not immediately adhere to a stationary path. Thus, in order to investigate if a system has a chaotic or phase space with attractors, we have to study the phase space after the ray has undergone a large number of transmissions and reflections. After a sufficient number of transmissions and reflections, we can evaluate if the ray has been stabilized into a stabile path or not. The number of the transmissions and reflections needed until a ray may adhere to a stable path depends on the refractive index ration n and the ratio between r and d .

The Matlab script *PSOS.m*²⁴ plots the phase space for the upper half of the left disk. *PSOS.m* can be found in the appendix. The PSOS for the disk system presented in Fig. 2.2 is

shown in Fig. 2.4. The start conditions are randomly selected at the upper half of the left disk with a random angle that is smaller than the critical angle and with a random rotation clockwise or counterclockwise. Visual inspection of the PSOSs in Fig.2.4 reveals stable islands. These stable islands are attractors, which are represented by a set of point in the PSOS that does not changes when the number of transmissions and reflections for each of the randomly started ray increases²⁹. The basin of attraction is the set of start conditions that lead the ray into the same attractor³⁰.

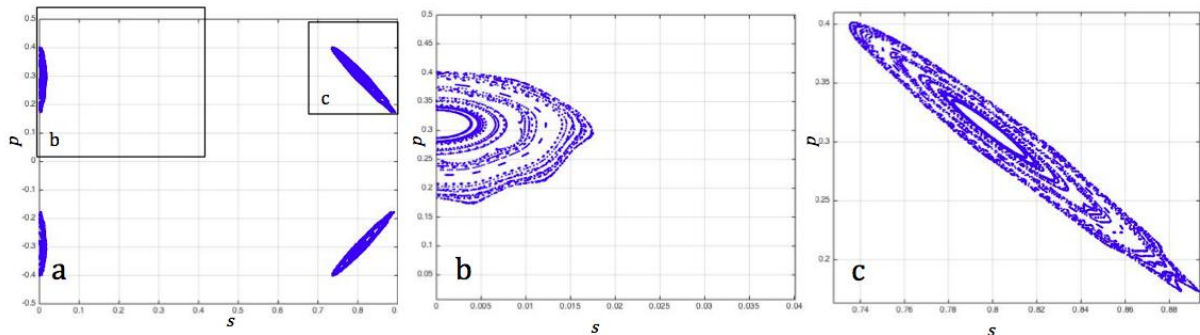


Figure 2.4 The PSOS for a two disk system with $r = d$ and $n = 1.9$. The regions marked in a) are enlarged in b) and c).

If the Matlab script *plot_ray.m*²⁴ runs for a higher number of transitions and reflections, the ray turns into the stationary regime, as already shown by Ryu and Hentschel²⁵ and expected from the phase space in Fig. 2.4. The stable islands are striking in Fig. 2.4b and Fig 2.4c.

Figure 2.5 and Fig. 2.6 show the stationary regime that is obtained when the ray shown in Fig. 2.3 is stabilized. The specific ray shown; needs 25 reflections and transmissions to find the stable circulation path. The two following figures plot shows the rays behavior in the attractor ray for 4000 to 6000 and 30 000 to 50 000 reflections and transmissions. As illustrated in the figures, the attractor has a structure of a fractal and is therefore a strange attractor²⁹. A fractal has self-similarity¹¹. When inspecting the attractor ray between 4000 to 6000 reflections and transmissions and resolving it until single trajectories can be seen (Fig. 2.5), the structure revealed is similar to the structure obtained when the same ray is resolved after 30 000 and 50 000 reflections and transmissions (Fig. 2.6). Thus, an enlarged area always shows same fractal structure¹¹ independent of how many long the ray is run.

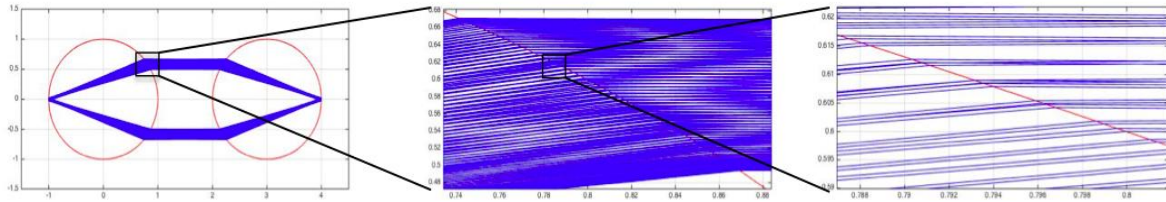


Figure 2.5 The ray's behavior in the space between 4000 and 6000 reflections and transmissions. The parameters s_0 , p , n , r and d are the same as for Fig. 2.3.

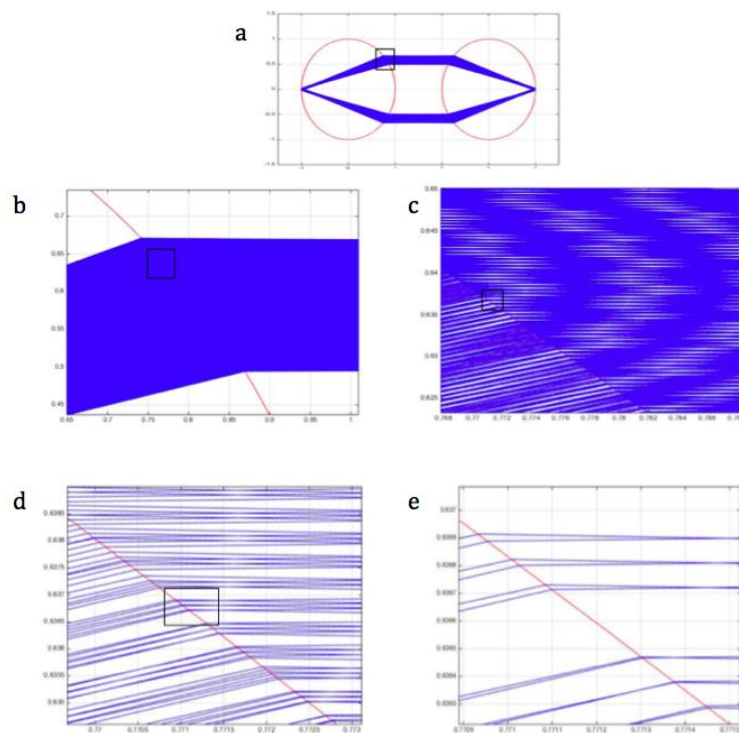


Figure 2.6 The ray's behavior in the space between 30 000 and 50 000 reflections and transmissions. The parameters s_0 , p , n , r and d are the same as for Fig. 2.3. The marked area in each plot is enlarged in the subsequent plot.

The start conditions affect which attractor a ray would stabilize into. Figure 2.7 shows different stationary regimes for different start conditions for two disks with the same refractive indices. These attractors correspond to different stable islands in the phase space.

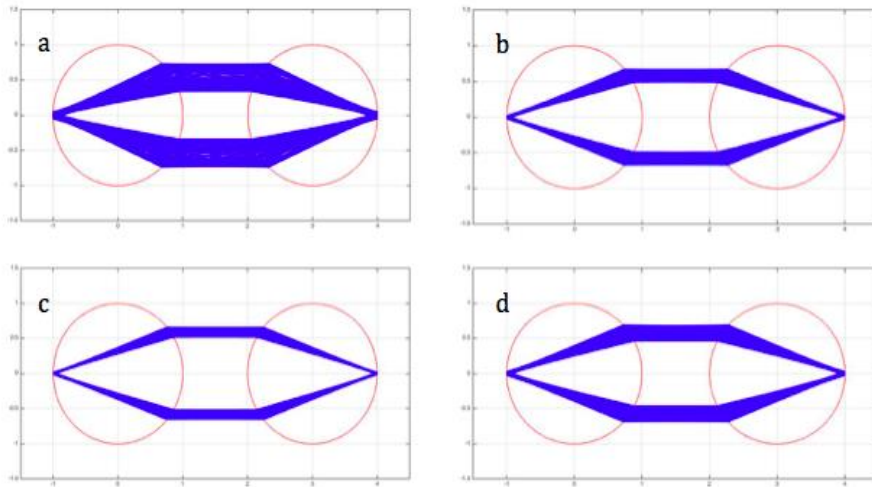


Figure 2.7 Different stable regimes for different start conditions for two disks with $r = d$ and $n = 1.9$, according to Fig 2.2. The start points for the figures are a) $s_0 = 0$ and $p_0 = 0.02$, b) $s_0 = 0.2$ and $p_0 = -0.3$, c) $s_0 = 0.3$ and $p_0 = 0.3$, d) $s_0 = 0.9$ and $p_0 = 0.1$. These plots are plotting the ray's behavior in the interval between 4000 and 6000 reflections and transmissions.

The stable regimes also change if we change the refractive index of the disks. This is because of the angle of refraction depends on the ratio between the refractive index of the disk and the media around the disks (according to Snell's law of refraction, i.e. Eq. 2-1).

Figure 2.8 illustrates how the stable regimes changes for a ray with the same start conditions but different refractive index of the disks.

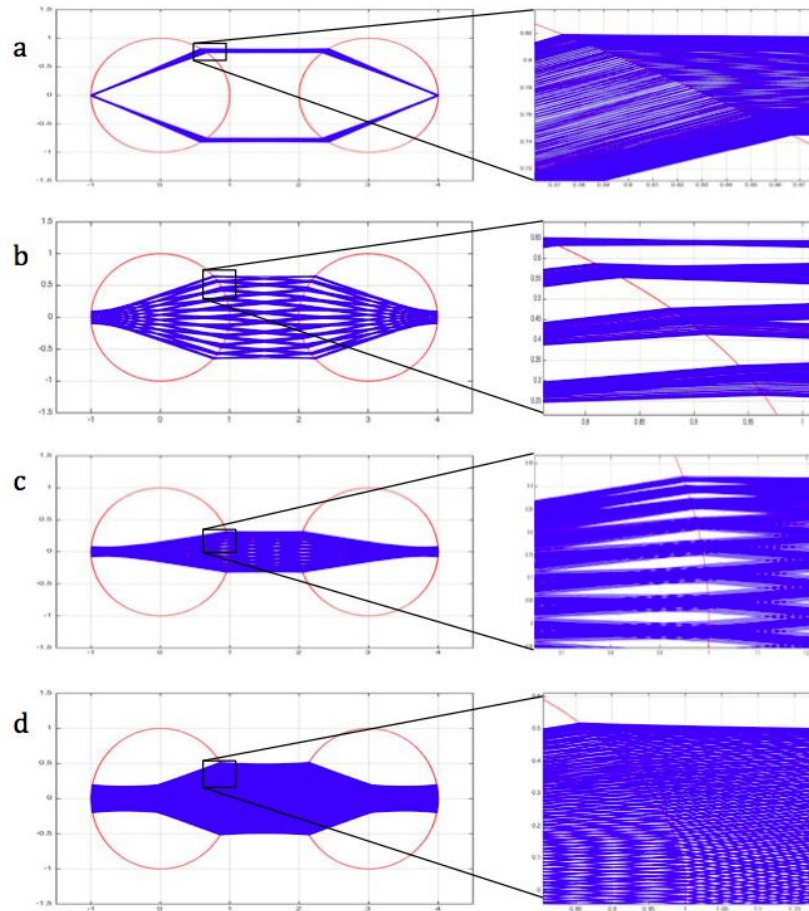


Figure 2.8 The stable rays that are in the basin of attractors for four cases with different refractive index of the disks. The start point of the ray is $s_0 = 0.3$ and $p_0 = 0.3$ and $r = d$ according to Fig. 2.2. The refractive index for the disks is a) $n = 1.8$, b) $n = 2.0$ c) $n = 2.2$ and d) $n = 3.0$.

As illustrated in Fig. 2.8 the attractor the ray leads into changes when the refractive ratio, n , changes. This change in the structure of single attractors leads to a change of the phase space of the disk system. This is illustrated in Fig. 2.9. The result of the attractors shown in this thesis are in accordance with the results shown by Ryu and Hentschel²⁵. As Fig. 2.9 illustrates, the width of the phase space in p -direction that is covered by trajectories is reduced with increasing refractive index n . The reason for this is that the maximum angle of incidence θ that allows transmissions from the inside to the outside of the disk reduces with increasing refractive index n . According to Eq. 2-1 and Eq. 2-3 the maximum momentum allowing transmission from the inside to the outside of the disk is $p < \frac{1}{n}$.

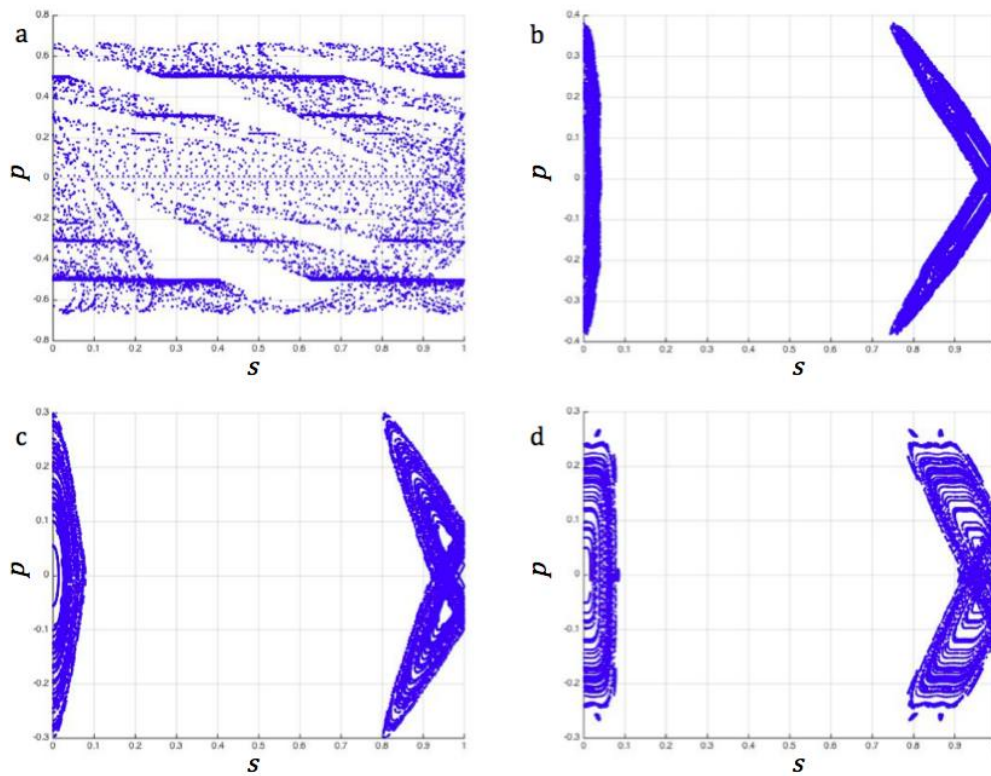


Figure 2.9 The PSOS for a two disk system with $r = d$. The refractive ratio of the two-disk system is a) $n = 1.5$, b) $n = 2.0$, c) $n = 2.5$ and d) $n = 3.0$.

By studying the PSOS in Fig. 2.9 closer, a rich variety of strange attractors can be found. We consider the example with $n = 2.0$ a bit closer. We inspected the stable islands in the PSOS of Fig. 2.9b and identified strange attractors. The start conditions for rays enclosing in attractors are indicated by squares in Fig. 2.10. The start conditions for one ray that leads to each of the attractors are listed in table 2.1. The different attractors are plotted in Fig 2.11.

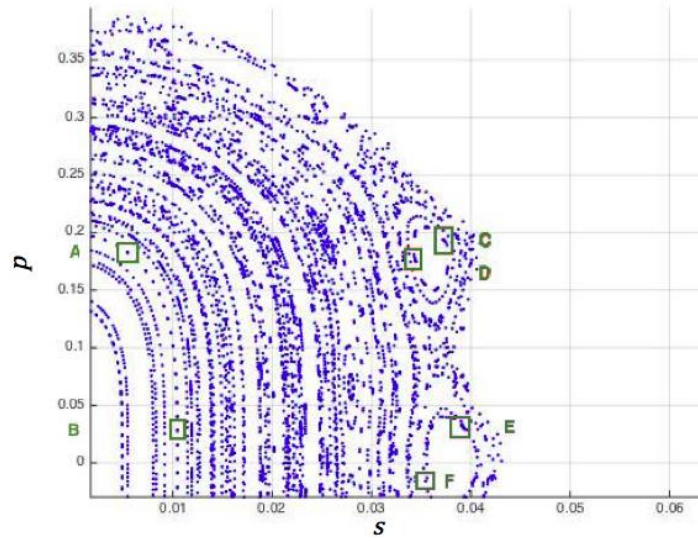


Figure 2.10 A closer view at the PSOS for $n = 2.0$ in Fig. 2.9. Some start condition for some attractors are indicated.

	s_0	p_0
A	0.005479	0.1825
B	0.01044	0.02787
C	0.03721	0.194
D	0.03441	0.1767
E	0.03908	0.03284
F	0.03544	-0.0158

Table 2.1 Start conditions for different stable orbits for $n = 2.0$ according to Fig 2.10.

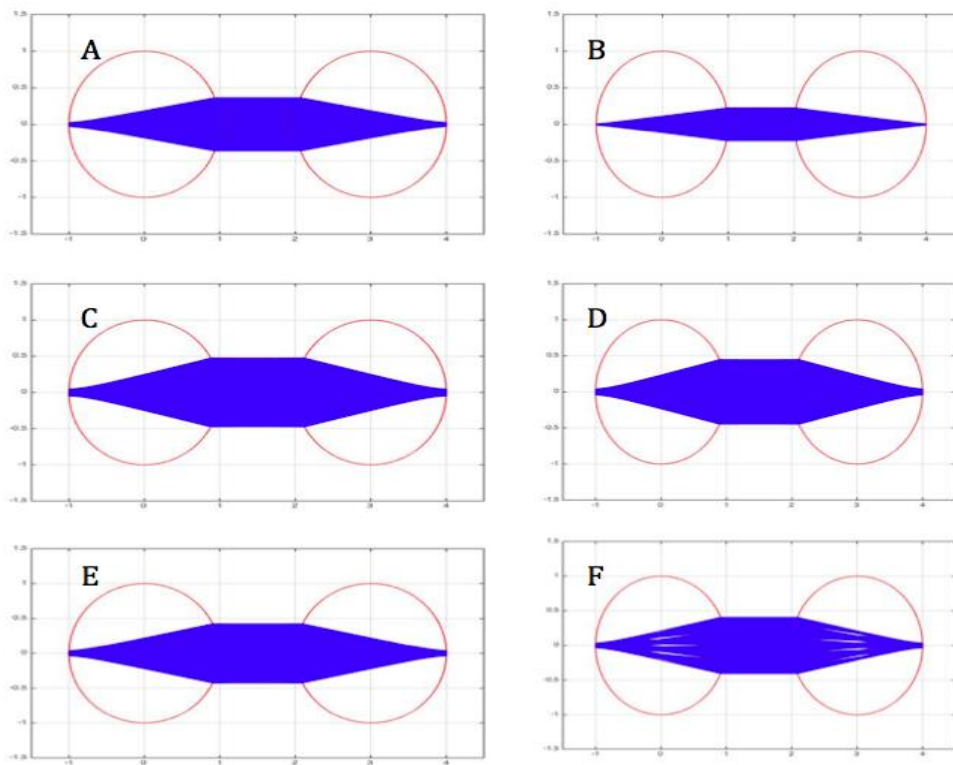


Figure 2.11 Plots of the 1000 first transmissions and reflections of a two-disk model with $r = d$ and $n = 2$. The start conditions are given in table 2.1.

As the previous figures confirm, a large variety of attractors can be found. The most simple of the stable regimes is shown in Fig. 2.12.

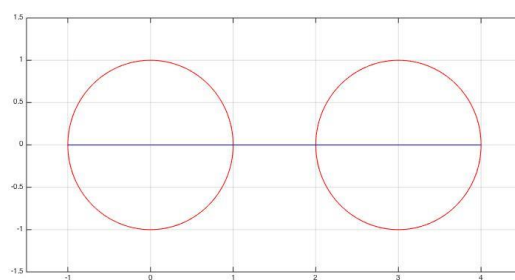


Figure 2.12 The most simple of the stable regimes is obtained for $s_0 = 0$ and $p_0 = 0$, with $r = d$ and $n = 1.9$. The behavior of the ray is plotted up to 3000 reflections or transmissions

Another obvious stable regime is given in Fig. 2.13. The start angle, θ , of this this periodic ray orbit can be found according to the following equation

$$\theta = \cos^{-1}\left(\frac{n_2}{2n_1}\right) \quad (2-4)$$

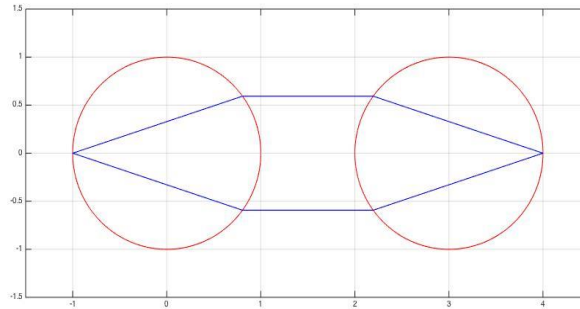


Figure 2.13 Another simple stable regime, $s_0 = 0$ and p_0 calculated in Eq. 2-4, with $r = d$ and $n = 1.9$. The behavior of the ray is plotted up to 3000 reflections or transmissions

The start position of this ray orbit is given by $s_0 = 0$. A consequence of Eq. 2-4 is that this ray exists for $n_1 = 1$, only if the refractive index of the disk, n_2 , is between $\sqrt{2}$ and 2.

As Fig. 2.9a shows, a chaotic phase space is obtained for a ratio of refractive indices equal to $n = 1.5$, while the phase space shown in Fig. 2.9b-d i.e. for $n = 2.0$, $n = 2.5$ and $n = 3.0$, respectively, a phase space with fractal attractors are obtained. Figure 2.14 illustrates the PSOS for different values of n in the interval where the PSOS changes from a chaotic phase space (Fig. 2.14a with $n=1.77$) to a phase space with fractal attractors. (Fig. 2.14b with $n=1.78$).

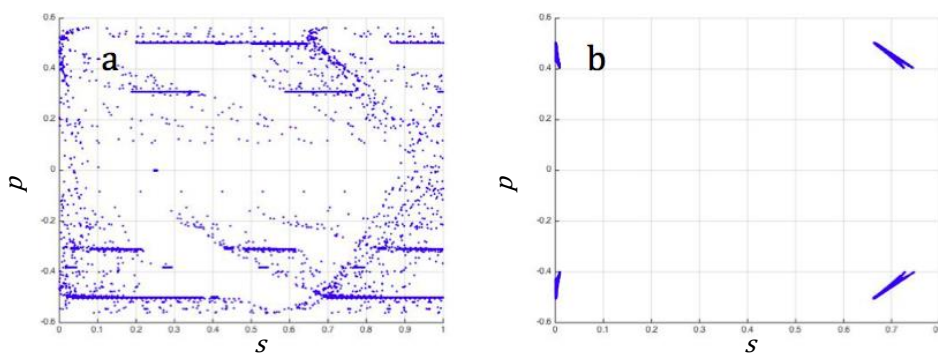


Figure 2.14 The PSOS for a two disk system where $r = d$, in a) $n = 1.77$ and in b) $n = 1.78$.

The phase space and the attractors of the system change also when the distance between the disks is changed as illustrated in Fig 2.15.

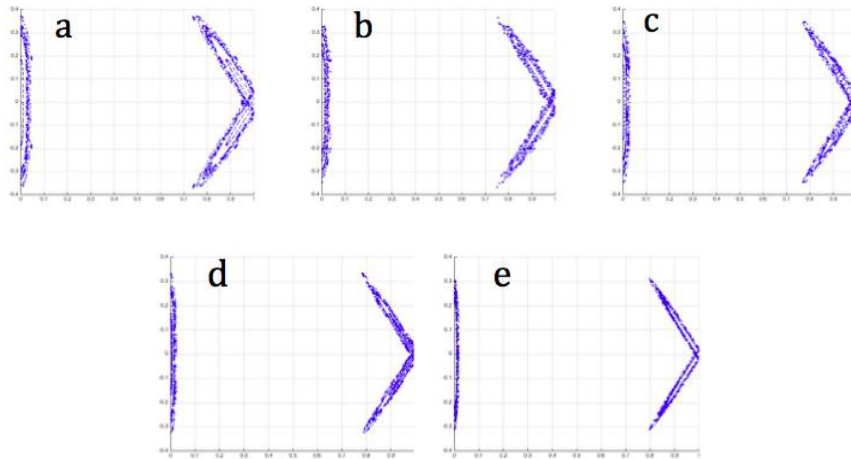


Figure 2.15 Phase space for a two-disk system with $n = 2.0$ and the relationship between r and d is a) $d = 0.5r$, b) $d = r$, c) $d = 2r$, d) $d = 3r$ and e) $d = 4r$.

Since dielectric resonant nanospheres are closely packed on Si (amorphous silicon) solar cells it is interesting to investigate the two-disk system with attached spheres, i.e. $d = 0$. Figure 2.16 and Fig. 2.17 shows such systems for two different refractive indices. Figure 2.18 and Fig. 2.19 show the phase space for these systems.

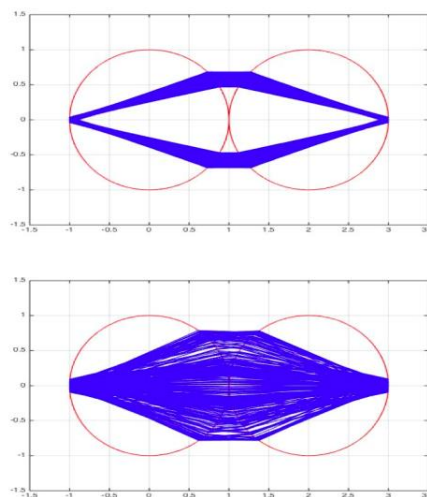


Figure 2.16 Attractors for a two disk system with $n = 1.9$. The start conditions for a ray that leads to each of the attractors is for the upper system is $s_0 = 0.4$ and $p_0 = 0.3$, and for the lower $s_0 = 0.2$ and $p_0 = -0.1$

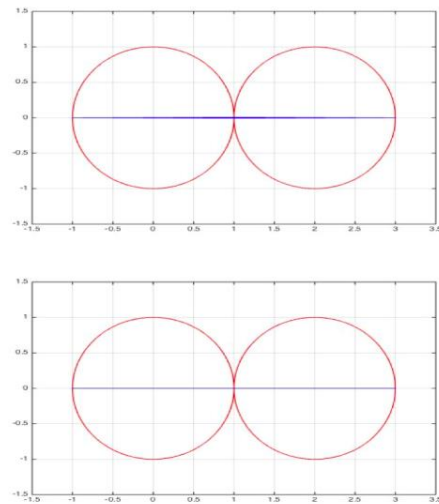


Figure 2.17 Attractors for a two-disk system with $n = 2.0$. The start conditions for a ray that leads to each of the attractors is for the upper system is $s_0 = 0.4$ and $p_0 = 0.3$, and for the lower $s_0 = 0.2$ and $p_0 = -0.1$

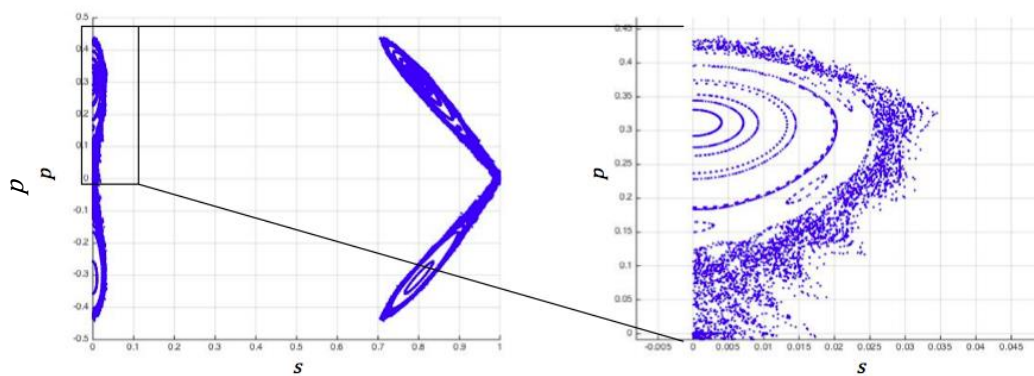


Figure 2.18 Phase space for a two-disk system with no distance between the disks, $n = 1.8$.

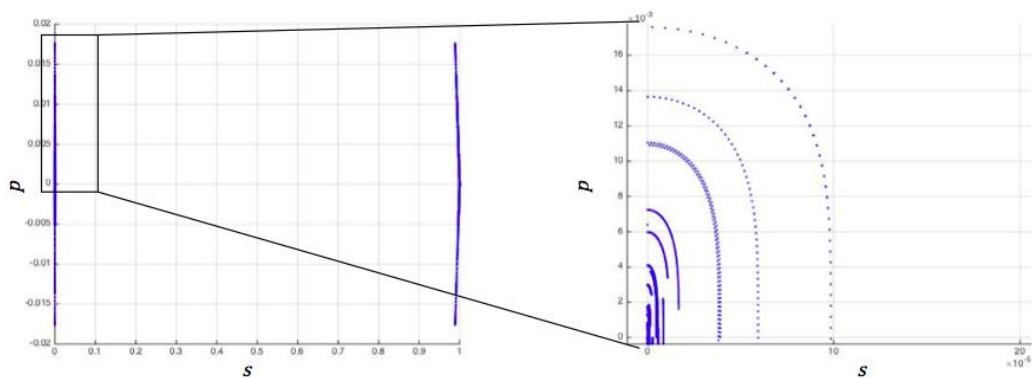


Figure 2.19 Phase space for a two-disk system with no distance between the disks, $n = 2.0$.

2.2 Ray dynamics in arrays of disks

While the focus of the investigation of the classical ray dynamics in coupled disks was put on two-disk systems, we will in this section shortly present results on systems containing more than two disks. As previously, we apply the deterministic selection rule. As in the previous chapter, we define r as the radius of the disks, d is the shortest distance between the disks and n is the ratio between the refractive index inside the disks and the refractive index of the regions outside the disks. The Matlab script *plot_ray.m*⁶ is used for investigating the ray dynamics. Figure 2.20 gives the attractors rays with different start conditions ahead for some systems with different number of disks and different n . In this figure the ray is plotted between 89 500 and 90 000 reflections or transmissions. The reason of this high number is to demonstrate that even after a long time, rays may not find a attractor.

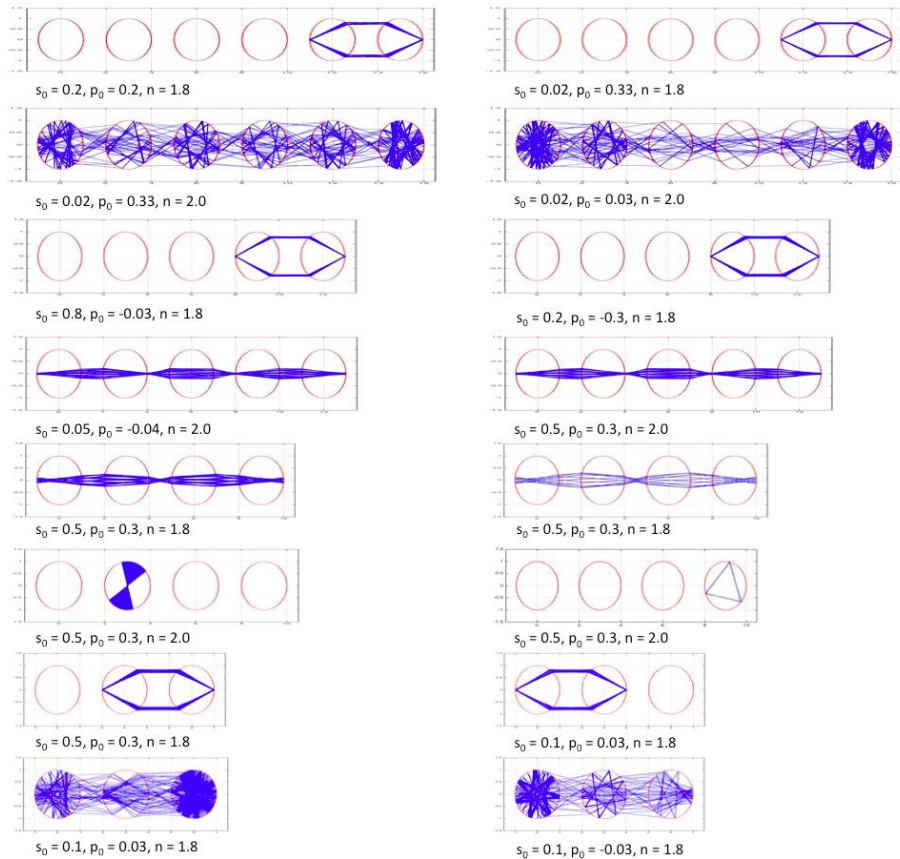


Figure 2.20 Disks systems that consist more than two disks. The start point and refractive index of the system is given for each attractor. The behavior of the ray is plotted in the space between 89 500 and 90 000 reflections or transmissions. The radius of the disks is equal the distance between the, i.e. $r = d$.

Figure 2.21 gives the PSOSs for systems with a different number of disks when the refractive index of the disks is $n = 1.78$. The Matlab script *PSOS.m*²⁴ was used to obtain the PSOS for the upper part of the left disk. This refractive index is close to the value where the chaotic phase space turned into a phase space with attractors as in Fig. 2.14.

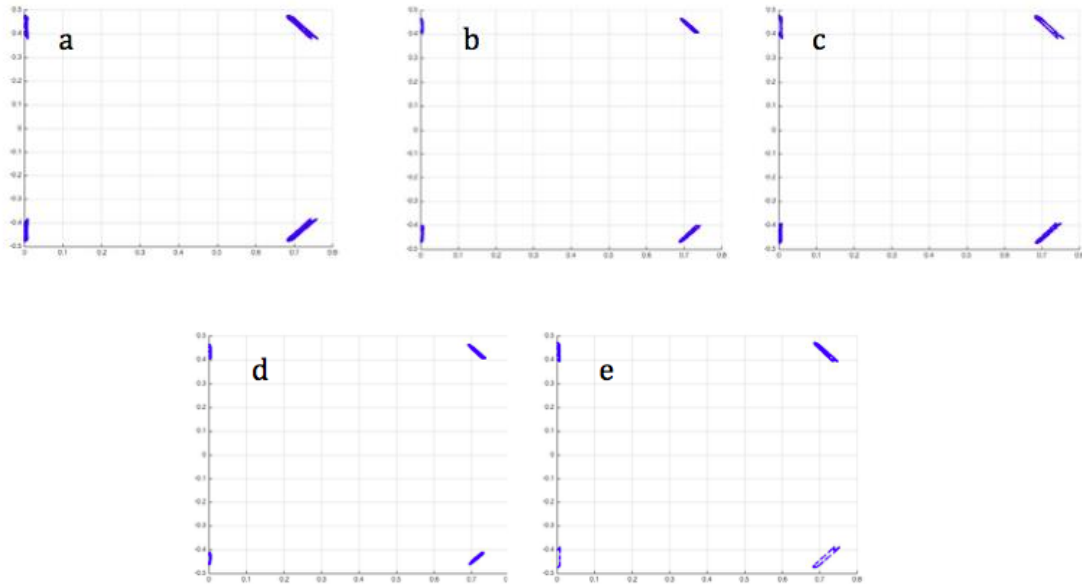


Figure 2.21 PSOS for systems with a) two disks, b) three disks, c) four disks, d) five disks and e) ten disks. The refractive index of the disks is $n = 1.8$.

Chapter 3

Plane wave scattering in disk systems

3.1 Resonances and whispering gallery modes in highly scattering systems

When light impinges on a scatterer, the light is scattered, transmitted in forward direction or absorbed. In this thesis, we do not consider the phenomenon absorption. The situation is illustrated in Fig. 3.1, where a plane wave (a) moves towards a spherical scatterer (b).

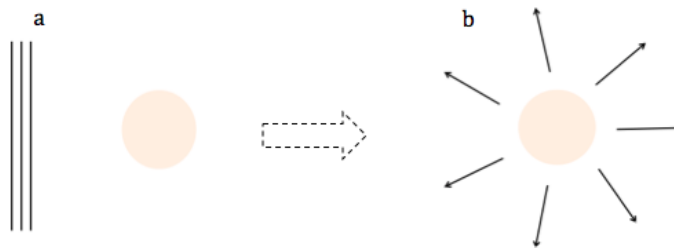


Figure 3.1 a) When light hits a non-absorbing scatterer, the wave is scattered or transmitted forward direction. This is illustrated by a plane wave (a) that moves from the right towards a scatterer (b)

The incoming plane wave is given by may be written as

$$\varphi(\vec{r}) = e^{i\vec{k}\vec{r}} \quad (3-1)$$

where $|\vec{k}| = k = \frac{2\pi}{\lambda}$ is the angular wavenumber, λ is the wavelength and \vec{r} is the position vector.

When the plan wave hits the scatterer, resonances may arise. This is illustrated in Fig. 3.2. Here we assume that the maxima shown in Fig. 3.2 refer to maxima of the wave function. Later we will show plots of the square of the absolute value of the wave function, where maxima of the square of the absolute value of the wave function refer to both maxima and minima of wave functions. Resonances as shown in Fig. 3.2 typically arise in wavelength regions, in which the wavelength of the electromagnetic radiation (in our case the plane wave) is approximately of the same order as the size of the scatterer. When the wavelength match approximately the size of the scatterer, the amount of scattered light is high¹⁰. In these wavelength regions, the appearance and the type of the resonances depends on the actual value of the angular wavenumber k , the geometry of the scatterer and the refractive index of the scatterer and the surrounding medium. In general, resonances display very diverse patterns. The resonances shown in Fig. 3.2 are called whispering gallery modes. These whispering gallery modes are described by Bessel functions of first order. For these resonances the energy is stored in the disks and we say, the light is trapped for a period of time. Whispering gallery modes are wave that are observed at concave surfaces. They name ‘whispering gallery modes’ derives from the study of sound waves that were observed in the whispering gallery of St Paul’s Cathedral in London²³. They are of high importance in different fields of physics.



Figure 3.2 Whispering gallery modes occurs for specific values of k .

The whispering gallery modes that are observed in wave mechanics correspond to certain rays as illustrated in Fig. 3.3. The rays are periodic rays that bounce a certain number of times inside the disk. In the actual case illustrated in Fig. 3.3 the number of bounces is six. This corresponds to six maxima of the wave function the disk. As the number of bounces increases or as the refractive index increases, the reflection inside the disk may be due to internal reflection.

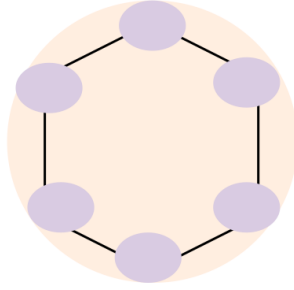


Figure 3.3 The number of reflections of a ray inside the disk corresponds approximately to the numbers of maxima of a wave function.

In first approximation, we expect that whispering gallery modes appear, when the optical length of a ray is a multiple of the wavelength of the incoming plane wave. The optical length, l_{eff} , is calculated as the actual length of the ray (geometrical length of the ray) weighted by the refractive index, n . We denote the multiplicity by N_j . Thus we obtain the relation (quantization rule)

$$N_j = \frac{l_{eff}}{\lambda_j} = \frac{l \cdot n}{\frac{2 \cdot \pi}{k_j}}, N \in \mathbb{N} \quad (3-2)$$

where λ_j is the wavelength and k_j is the angular wavenumber. As N increases, the optical length of the resonant modes approach the circumference of the disk as illustrated in Fig. 3.3.

These same considerations are assumed to apply for the attractors described in chapter 2. It is assumed that attractor rays correspond to resonant modes in the two-disk wave system²⁵ For the simple attractor shown in Fig. 2.12, the optical length for a ray moving from left to right (or opposite) is given by

$$l_{eff} = n_1 d + 4r n_2 \quad (3-3)$$

where d is the distance between the disks, r is the radius of the disks, n_1 and n_2 are the refractive indices of the surrounding medium and the disks, respectively.

3.2 Plane-wave scattering algorithm

For the two-disk system shown in Fig. 3.4, two wave equations have to be fulfilled: One wave equations for the area surrounding the disks and one wave equation for the area inside the disks. These wave equations are given in the equations below.

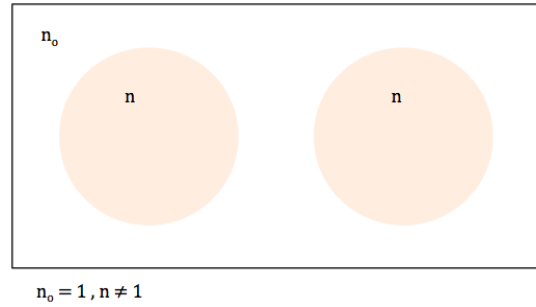


Figure 3.4 A two-disk system with a refractive index n surrounded by a medium with refractive index $n_0 = 1$.

$$\text{Outside: } \Delta\psi + k^2\psi = 0 \quad (3-4)$$

$$\text{Inside: } \Delta\psi + k^2(n(\vec{r}))^2\psi = 0 \quad (3-5)$$

where ψ is the wave function, k is the angular wave number, $n(\vec{r})$ is the refractive index of the disks and \vec{r} is the position vector. We assume that the refractive index in the area surrounding the disks equals one. It can be easily shown that these equations are equivalent to the

$$-\Delta\psi + V(\vec{r})\psi = k^2\psi \quad (3-6)$$

Where k is the angular wave number, \vec{r} is the position vector and $V(\vec{r})$ is the potential of the system given by

$$V(\vec{r}) = k^2 \cdot v(\vec{r}) \quad (3-7)$$

The function $v(\vec{r})$ is given as

$$v(\vec{r}) = \begin{cases} (1 - (n(\vec{r}))^2), & \text{inside disk} \\ 0, & \text{outside disk } (n = 1) \end{cases} \quad (3-8)$$

where $n(\vec{r})$ is the refractive index of the disks. Eq. 3-6 can be written as

$$[-\Delta + V(\vec{r})]\psi = k^2\psi \quad (3-9)$$

The scatter problem of a plane wave being scatter at two or more scatterers can be solved by the Lippmann-Schwinger equation²¹. The Lippmann-Schwinger equation writes as

$$\psi(\vec{r}) = \varphi(\vec{r}) - \int G(\vec{r}, \vec{r}', k) V(\vec{r}') \psi(\vec{r}') d^2\vec{r}' \quad (3-10)$$

where $\psi(\vec{r})$ is the solution for the wave function in the potential $V(\vec{r})$, $\varphi(\vec{r})$ is the solution of the free Schrödinger equation, $V(\vec{r})$ is the potential as described in Eq. 3-7 and \vec{r} is the position vector and $G(\vec{r}, \vec{r}', k)$ is the Green function for Helmholtz equation, given by

$$(\Delta + k^2) G(\vec{r}, \vec{r}', k) = -\delta(\vec{r} - \vec{r}') \quad (3-11)$$

where $\delta(\vec{r} - \vec{r}')$ is the delta function and k is the angular wavenumber. . It can easily be proven that the Lippmann-Schwinger equation is a solution of Eq. 3-9. For the proof it can to be used that $\varphi(\vec{r})$ is a solution of the free Schrödinger equation

$$(\Delta + k^2)\varphi = 0 \quad (3-12)$$

For this special case, the Green function is given by¹⁸

$$G(\vec{r}, \vec{r}', k) = \frac{i}{4} H_0^{(+)}(k|\vec{r}' - \vec{r}|) \quad (3-13)$$

where $H_0^{(+)}$ is the Hankel function of first kind of zero order, given by

$$H_0^{(+)}(x) = J_0(x) + iV_0(x) \quad (3-14)$$

where $J_0(x)$ is the Bessel function of first kind of zero order and $V_0(x)$ is the Bessel function of second kind of zero order. The incoming wave is now represented by the plane wave in Eq. 3-1. This leads to the following explicit equation for $\psi(\vec{r})$ ¹⁸

$$\psi(\vec{r}) = e^{i\vec{k}\vec{r}} - i\frac{k^2}{4} \int H_0^{(+)}(k|\vec{r}' - \vec{r}|) v(\vec{r}') \psi(\vec{r}') d^2\vec{r}' \quad (3-15)$$

In order to turn Eq. 3.15 into a form that can be implemented numerically we discretize the two-dimensional plane into a lattice structure as illustrated in Fig. 3.5.

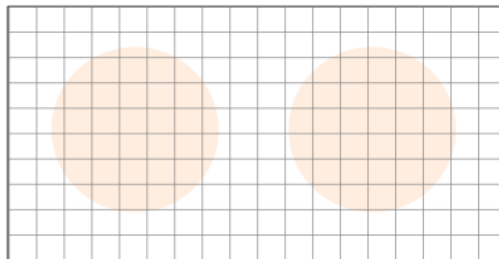


Figure 3.5 The plane is divided in a lattice structure in the Matlab scrip *Diskscattering_20082015.m*.⁶

For the discretization, we write Eq. 3.14 as

$$\psi(\vec{r}_j) = e^{ik\vec{r}_j} - i \frac{k^2}{4} \sum_{m=1}^N H_0^{(+)}(k|\vec{r}_m - \vec{r}_j|) v(\vec{r}_m) \psi(\vec{r}_m) \Delta A \quad (3-16)$$

where the continuous position vectors are turned into a discrete position vectors, i.e. $\vec{r} \rightarrow \vec{r}_m$ and $\vec{r}' \rightarrow \vec{r}_j$. We denote by N the total number of squares and ΔA the area of square each square in the lattice structure. Eq. 3-16 can be rewritten as

$$\psi_j = I_{j,m} \cdot \psi_m = e^{ik\vec{r}_j} - i \frac{k^2}{4} \Delta A \cdot G_{j,m} \cdot v_m \cdot \psi_m \quad (3-17)$$

where $I_{j,m}$ is the (j,m) element in the identity matrix. This can be summarized in matrix form to

$$\mathbf{M} \vec{\Psi} = \vec{R} \quad (3-18)$$

where the matrix \mathbf{M} is

$$\mathbf{M} = \mathbf{I} + i \frac{k^2 \Delta A}{4} \tilde{\mathbf{G}} \quad (3-19)$$

an element in the matrix $\tilde{\mathbf{G}}$ is given by

$$\tilde{G}_{j,m} = G_{j,m} v_m \quad (3-20)$$

and \vec{R} is

$$\vec{R} = \begin{pmatrix} e^{i\vec{k}\vec{r}_1} \\ \vdots \\ e^{i\vec{k}\vec{r}_j} \end{pmatrix} \quad (3-21)$$

By solving Eq. 3.18 for $\vec{\Psi}$, it is possible to calculate $\vec{\Psi}$.

The basic algorithm for the plane-wave scatter algorithm was developed by A. Kohler and R. Blümel prior to the start of this master thesis. It was implemented in the Matlab script *Diskscattering_20082015.m*⁶, which is attached in the appendix.

3.3 Plane-wave scattering in two-disk systems

In order to study the scattering of a plane wave at two equally sized disks we run the Matlab script *Diskscattering_20082015.m*⁶ using the potential as given in Eq. 3-7 and Eq. 3-7. If not otherwise stated we will use a radius 10.0 μm for both disks. This corresponds to a wavenumber of 1000 cm^{-1} , which is located in the mid-infrared region of electromagnetic radiation (wavenumbers are calculated as $\nu = \frac{1}{\lambda}$). In the following we will therefore screen wavenumber regions around this wavenumber, namely from around 500 cm^{-1} to 1400 cm^{-1} . The distance between the disks was set to zero. Figure 3.6 shows the potential for a two-disk system, where the refractive index of the disks is 2.0. Throughout this thesis, we used 50 grid points for the discretization of 20.0 μm in both x -direction y -direction. i.e. 50 grid points for the discretization of the diameter of the disks in x -direction and y -direction. This discretization led to a good resolution, while at the same time the computation time was such that simulations over large wavelength regions were possible. Simulations were done at the compute cluster at UiT - The Arctic University, the Linux Cluster Stallo, one of the Notur hardware resources, located in Tromsø²⁸.

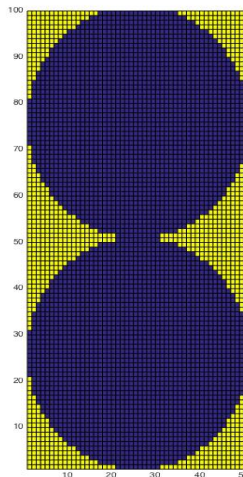


Figure Feil! Det er ingen tekst med den angitte stilen i dokumentet..1 Schematic view of the potential given by the two-disk system used in the Matlab script *Diskscattering_20082015.m*.

In the following, large wavenumber regions were screened for resonant modes. For each wavenumber the wave functions were calculated by using the Matlab script *Diskscattering_20082015.m*⁶. In order to detect resonant modes, we calculated for each wave function the integral over the absolute square of the wave function $|\vec{\Psi}|^2$. Figures 3.7-3.14 shows graph of the integral over the absolute square of the wave function $|\vec{\Psi}|^2$ as

disk system. Figures 3.7-3.14 correspond to different refractive indices. The respective refractive indices are given in the figure captions. From the graphs, it can be clearly seen that certain wavenumbers lead to peaks in the integral over the absolute square of the wave functions $|\bar{\Psi}|^2$. Where these peaks appear, depends also on the refractive index employed for the disks. In addition, Figures 3.7-3.14 display for each peak, the element-wise squared wave function $|\vec{\psi}_j|^2$ in insets in proximity to the peaks. In Figures 3.7-3.14, the incoming plan wave is coming from the top of the systems.

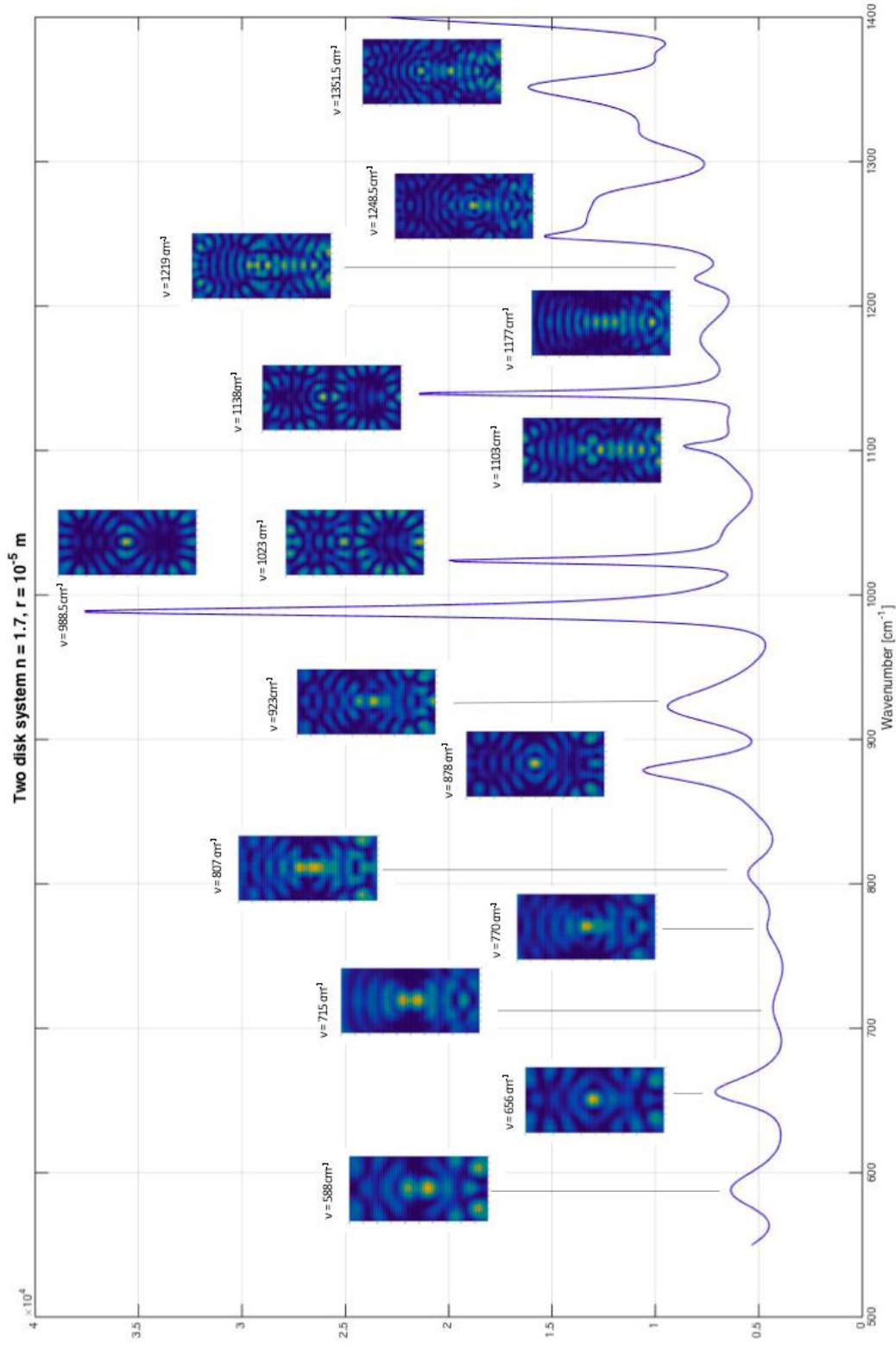


Figure 3.7 The integral over the absolute square of the wave function $|\bar{\Psi}|^2$ as a function of the wavenumber for a two-disk system with a refractive index equal $n=1.7$. For each peak the absolute square of the wave function $|\bar{\Psi}_j|^2$ is plotted. The radius of each disk is $10 \mu\text{m}$.

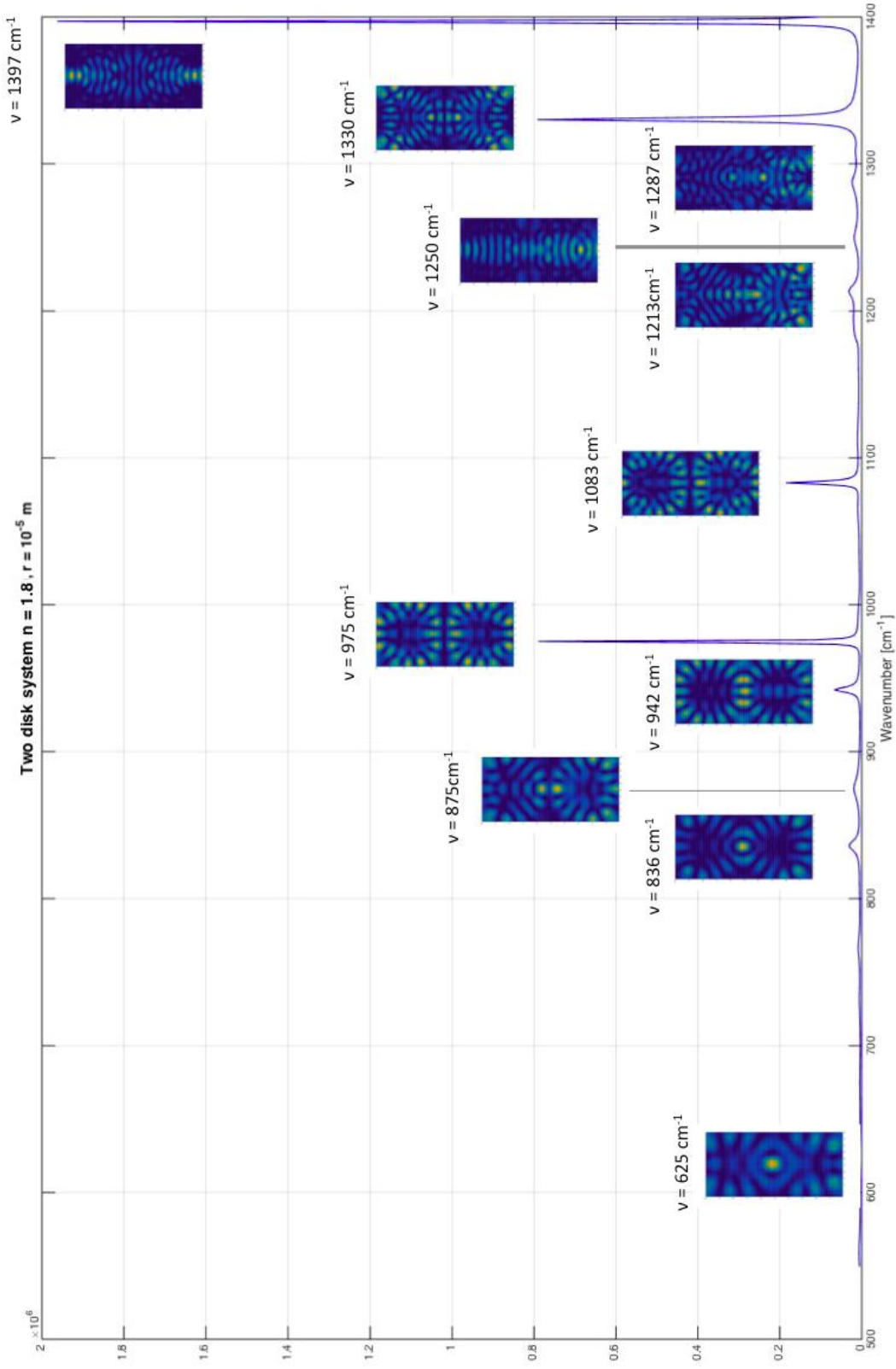


Figure 3.8 The integral over the absolute square of the wave function $|\bar{\Psi}|^2$ as a function of the wavenumber for a two-disk system with a refractive index equal $n=1.8$. For each peak the absolute square of the wave function $|\bar{\psi}_j|^2$ is plotted. The radius of each disk is $10 \mu\text{m}$.

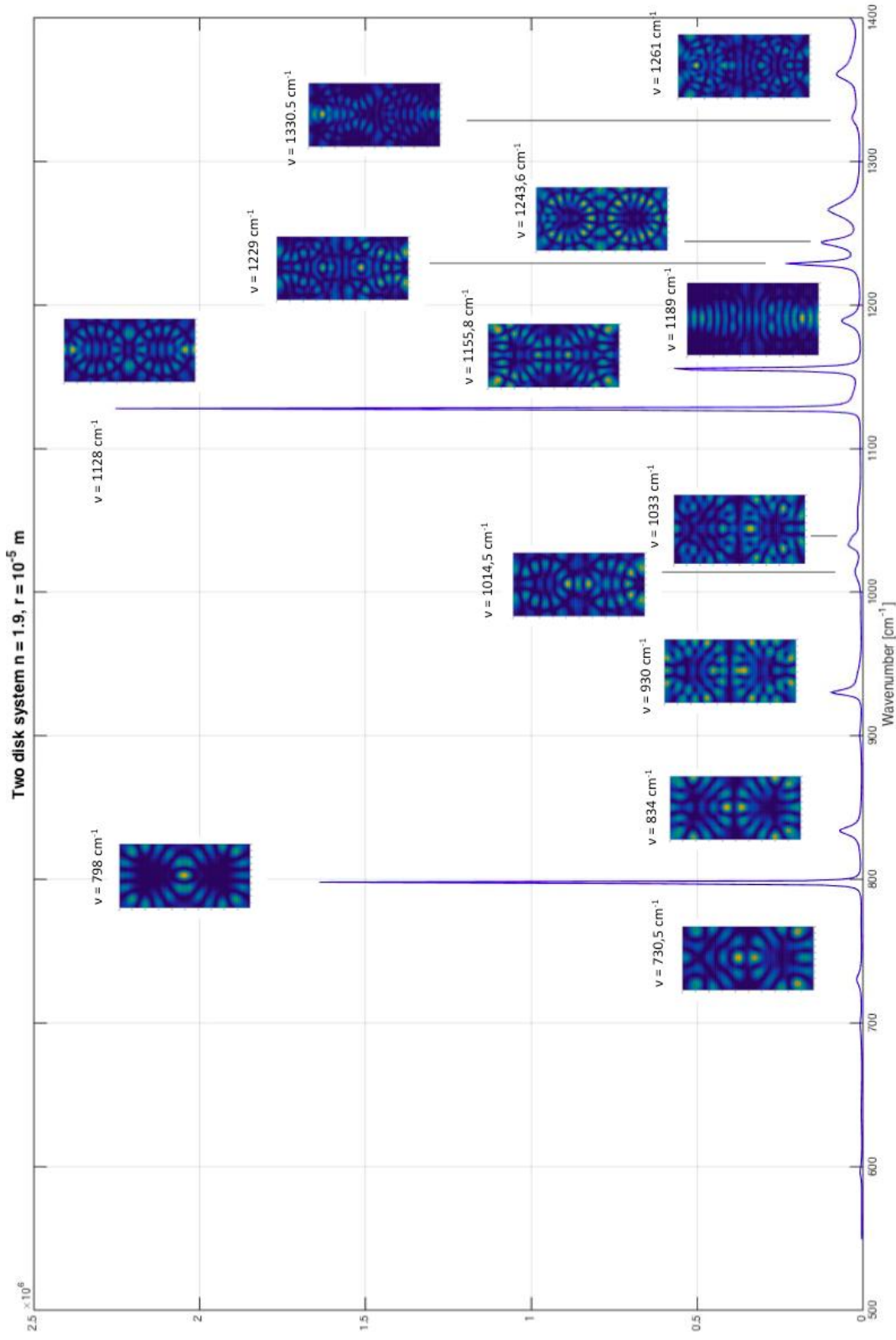


Figure 3.9 The integral over the absolute square of the wave function $|\bar{\Psi}|^2$ as a function of the wavenumber for a two-disk system with a refractive index equal $n=1.9$. For each peak the absolute square of the wave function $|\bar{\psi}_j|^2$ is plotted. The radius of each disk is $10 \mu\text{m}$.

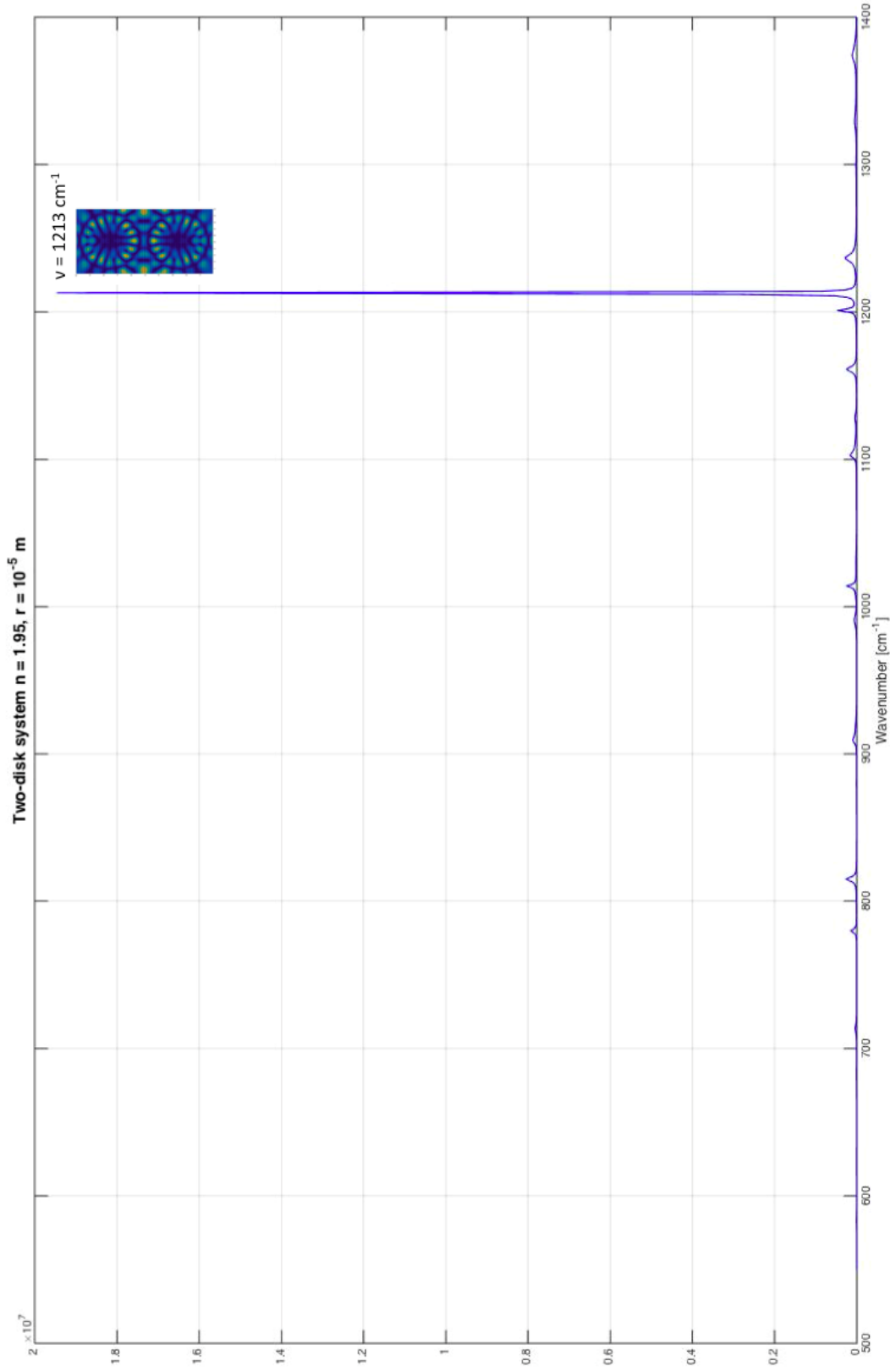


Figure 3.10 The integral over the absolute square of the wave function $|\bar{\Psi}|^2$ as a function of the wavenumber for a two-disk system with a refractive index equal $n=1.95$. For each peak the absolute square of the wave function $|\bar{\psi}_j|^2$ is plotted. The radius of each disk is $10 \mu\text{m}$

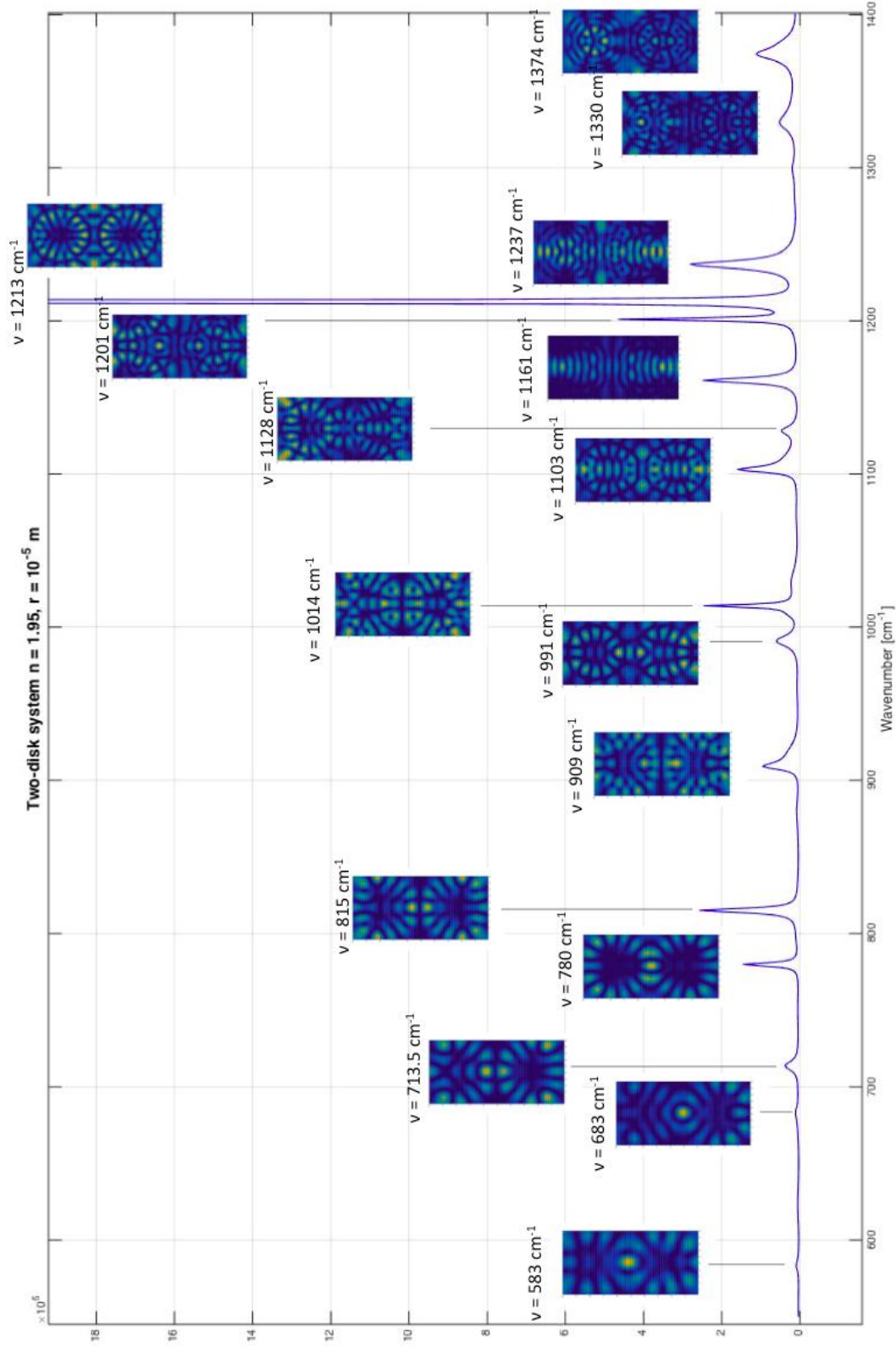


Figure 3.11 The integral over the absolute square of the wave function $|\bar{\Psi}|^2$ as a function of the wavenumber for a two-disk system with a refractive index equal $n=1.95$. For each peak the absolute square of the wave function $|\bar{\psi}_j|^2$ is plotted. The radius of each disk is $10 \mu\text{m}$

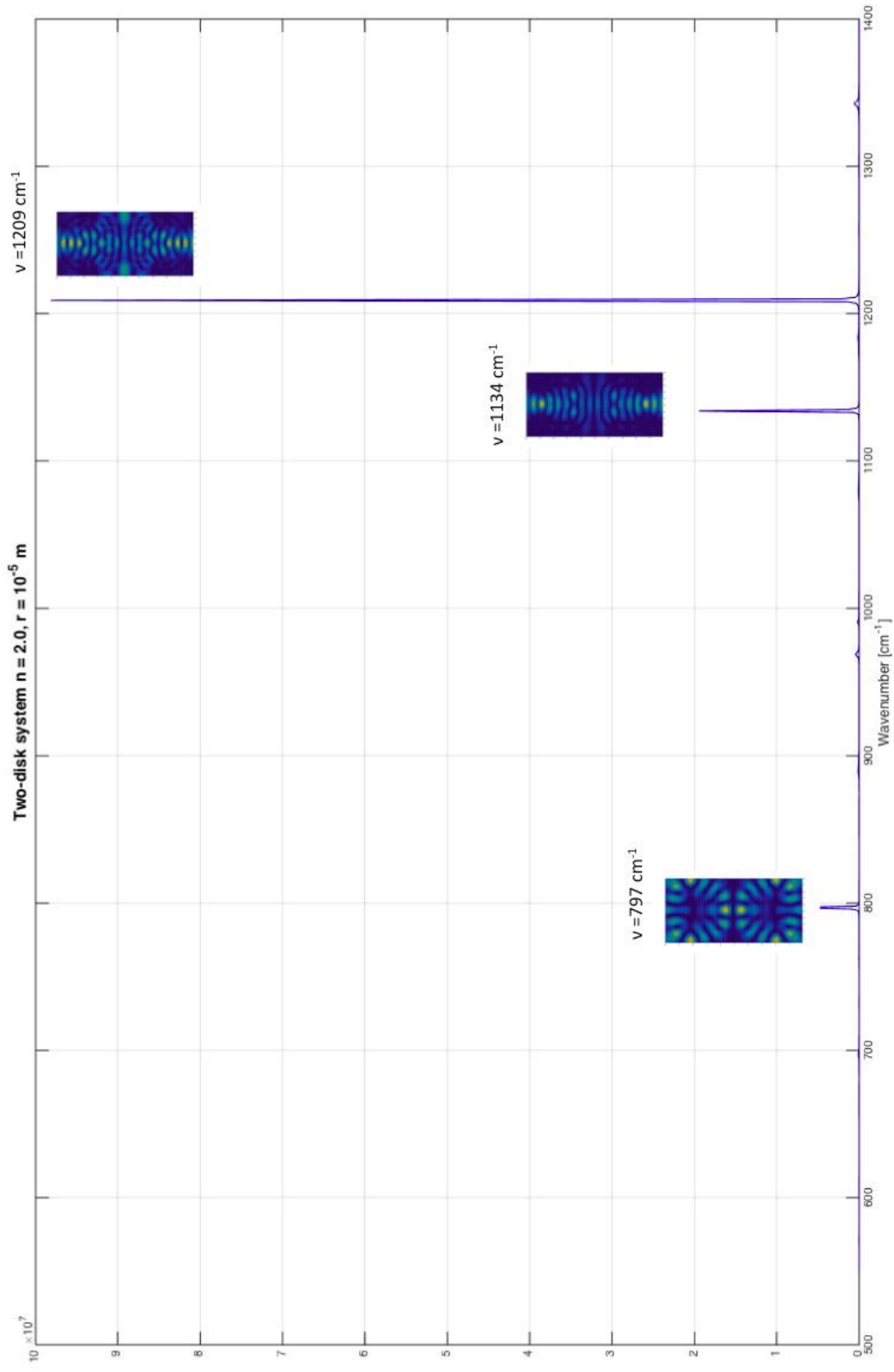


Figure 3.12 The integral over the absolute square of the wave function $|\bar{\Psi}|^2$ as a function of the wavenumber for a two-disk system with a refractive index equal $n=2.0$. For each peak the absolute square of the wave function $|\bar{\psi}_{\vec{j}}|^2$ is plotted. The radius of each disk is $10 \mu\text{m}$.

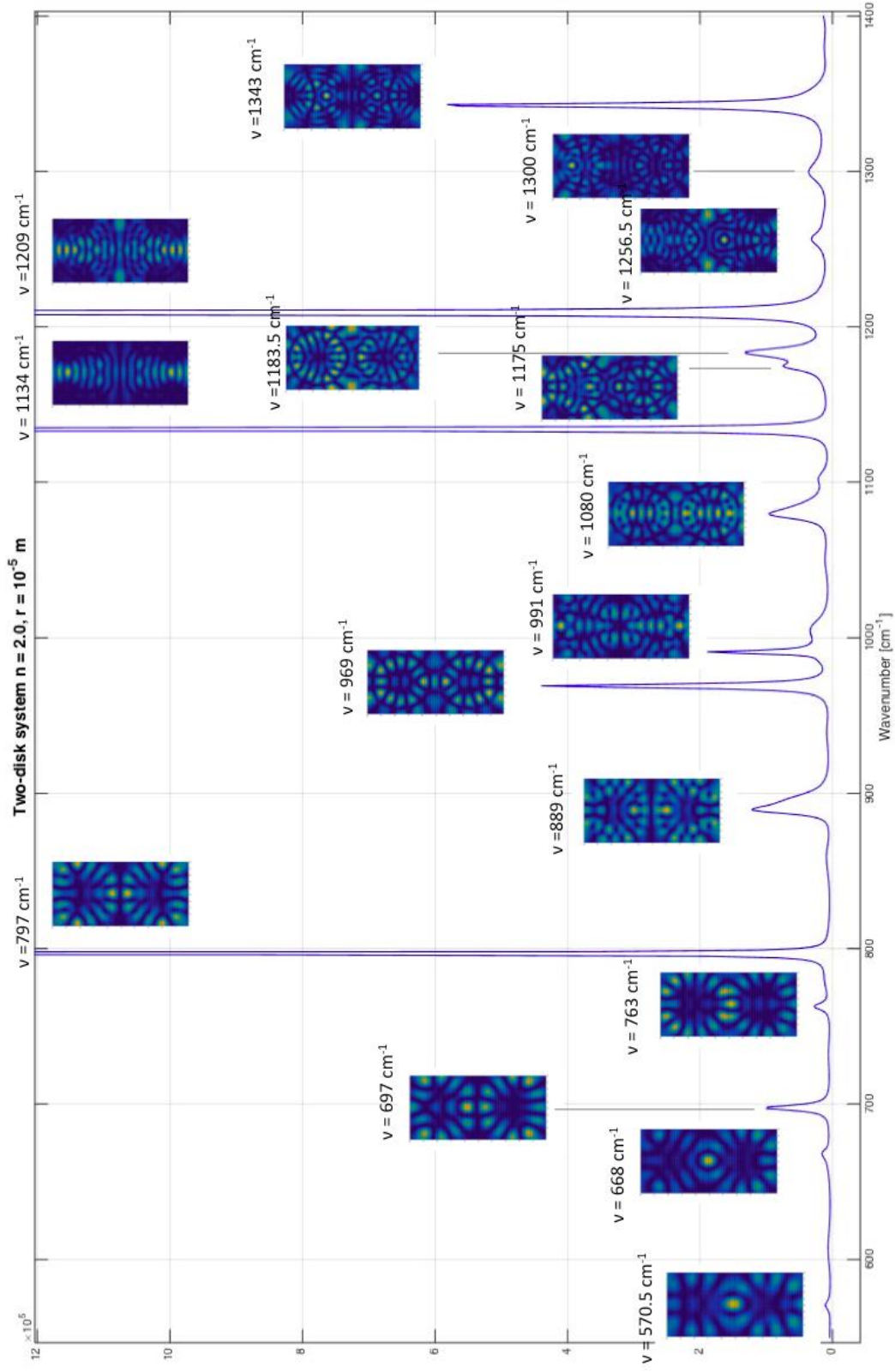


Figure 3.13 The integral over the absolute square of the wave function $|\bar{\Psi}|^2$ as a function of the wavenumber for a two-disk system with a refractive index equal $n=2.0$. For each peak the absolute square of the wave function $|\bar{\psi}_j|^2$ is plotted. The radius of each disk is $10 \mu\text{m}$.

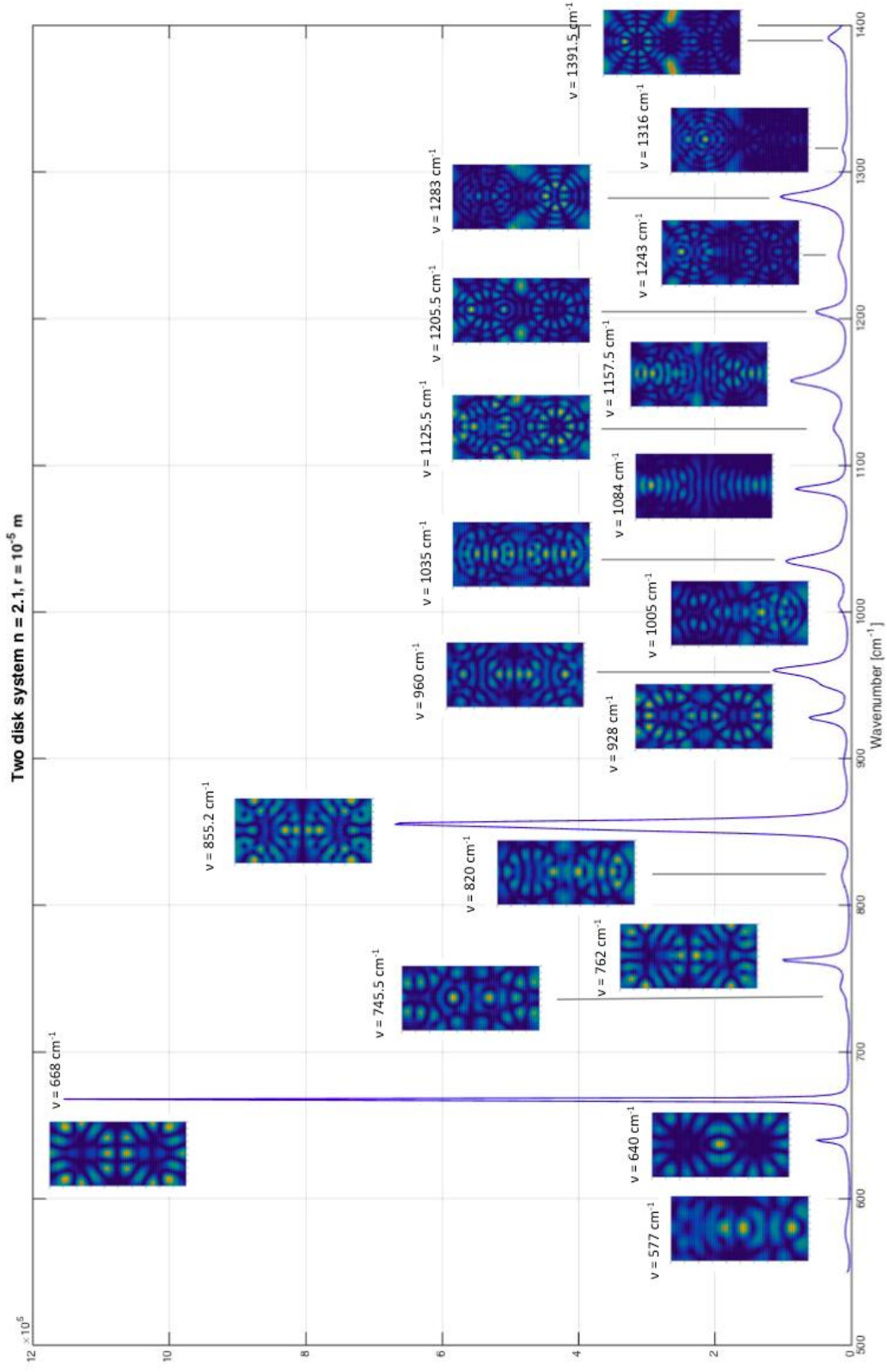


Figure 3.14 The integral over the absolute square of the wave function $|\bar{\Psi}|^2$ as a function of the wavenumber for a two-disk system with a refractive index equal $n=2.1$. For each peak the absolute square of the wave function $|\bar{\psi}_j|^2$ is plotted. The radius of each disk is $10 \mu\text{m}$.

When the wave functions for two-disk systems with refractive indices equal 1.8 or higher (i.e. with a phase space with stable islands) were evaluated, the resonance mode type displayed as squared absolute wave function in Fig. 3.15 existed in all cases. Since the squared absolute value of the wave function is displayed, both maxima and minima are indicated as maxima. In the two-disk central ray shown in Fig. 3.15, there are totally 18 maxima, which correspond to nine wavelengths. We associated the wave function in Fig. 3.15 with the ray shown in Fig. 2.12 and calculated the optical length of this ray according to Eq. 3-3 and compared the optical length with the wavelength were this resonance mode type appeared according to the quantization rule of Eq. 3-2 (see table 3.1). The quantization rule of Eq. 3-2 gave approximately $N = 9$ for all of the refractive indices (see table 3.1).

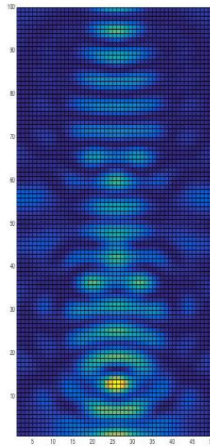


Figure 3.15 The square of absolute value of the wave function for wavenumber equal 1250 cm^{-1} for a two-disk system with a refractive index 1.8. We associate this resonant mode type with the ray shown in Fig. 2.12.

Refractive index	Wavenumber [cm ⁻¹]	N
1.8	1250	9.0
1.9	1189	9.04
1.95	1161	9.06
2.0	1134	9.07
2.1	1084	9.11

Table 3.1 The wavenumber in the first column corresponds to the wavenumber where the resonant mode type of Fig. 3.15 appears. The number of wavelengths, N , is calculated according to Eq. 3.2.

In the Figs. 3.7-3.14, a variety of whispering gallery modes with 12, 14 and 16 maxima (this indicates 6, 7 or 8 wavelengths inside, as explained in last paragraph) can be found. The whispering gallery modes that occur for the different refractive indices are given in table 3.2.

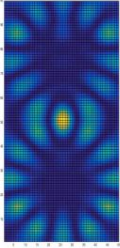
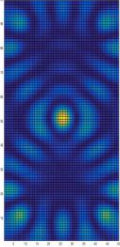
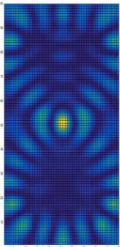
Whispering gallery modes	Refractive index	Wavenumber [cm ⁻¹]
12 	2.1	640
14 	1.8	836
	1.9	798
	1.95	780
	2.0	763
16 	1.7	998.5
	1.8	942

Table 3.2 Whispering gallery modes in the Fig. 3.7-14.

At the contact point between the two disks the coupling of the disks is large. The whispering gallery modes in the two disks are in phase, as the plots in table 3.2 shows. This coherent superposition at the touching point sums up in phase leading to an enhancement factor four in $|\bar{\Psi}|^2$.

3.4 Plane-wave scattering in three-disk system

The graph in Fig. 3.16 shows the integral over the absolute square of the wave function for the wavenumber region 800 cm^{-1} to 1200 cm^{-1} for a three-disk system. The radius of the disks is set to $10.0 \text{ }\mu\text{m}$, which is chosen to be the radius for all disks if nothing else is stated. The distance between the disks is zero. As for the previous section, the squared absolute value of the wave function is shown for the peaks. The superposition at the touching points can also be observed for three-disk system. According to the results from section 2.2, it is expected that the coupling between the disks is more complex than for a two-disk system. In the Fig. 3.16 the incoming plan wave is coming from the top of the system.

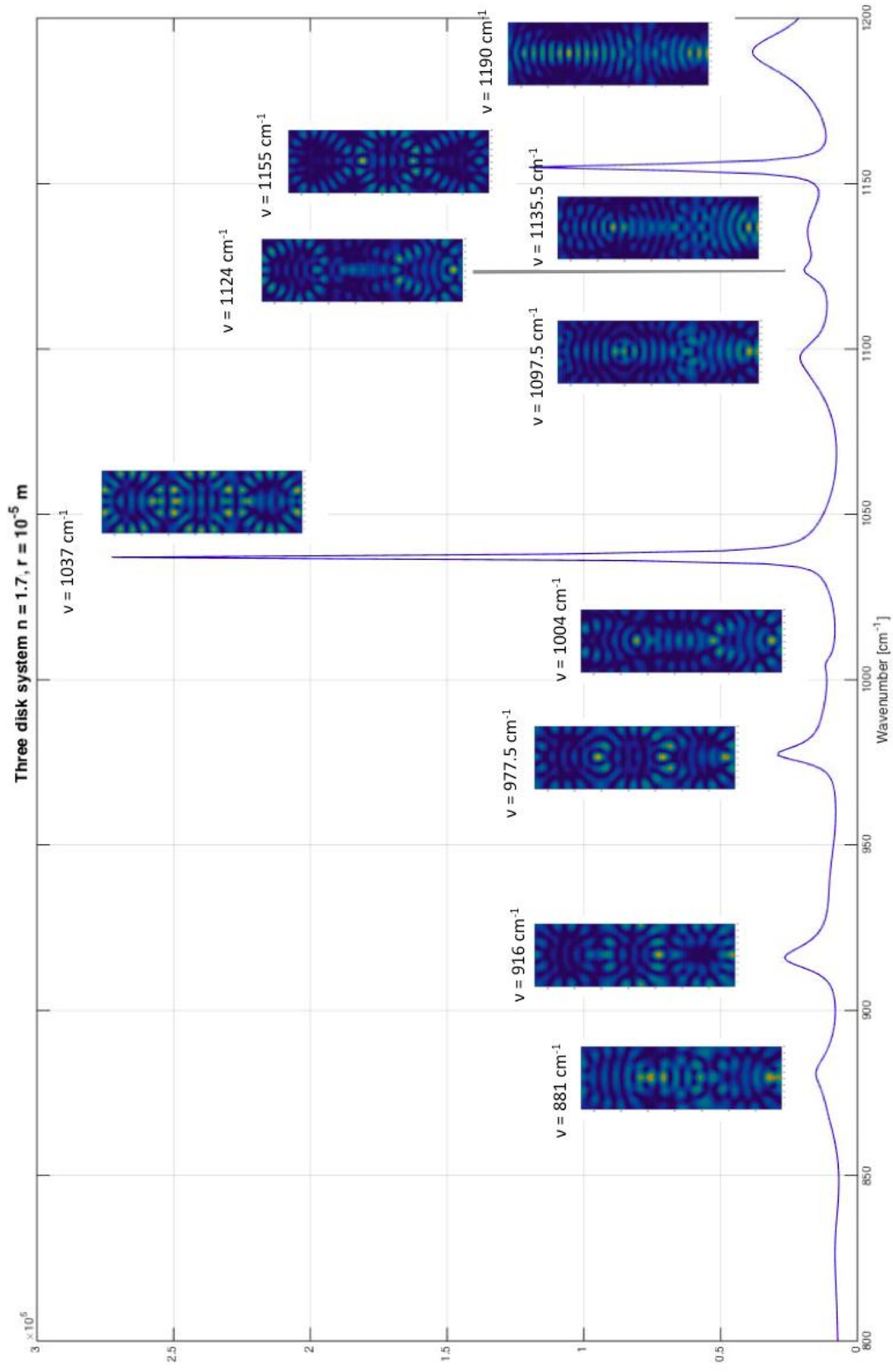


Figure 3.16 The integral over the absolute square of the wave function $|\bar{\Psi}|^2$ as a function of the wavenumber for a three-disk system with a refractive index equal $n = 1.7$. For each peak the absolute square of the wave function $|\bar{\psi}_j|^2$ is plotted. The radius of each disk is $10 \mu\text{m}$

3.5 Plane-wave scattering in two-disk system with differently sized disks

The Matlab script *DiskScattering_20082015.m*⁶ was modified to allow for systems of disks with different radius. An example is shown in Fig. 3.17, where the upper disk has a radius of 5 μm and the lower disk has a radius of 10 μm . As refractive index we used $n=1.9$.

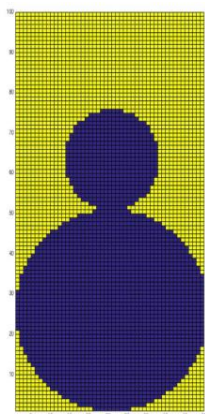


Figure 3.17 A schematic view of the potential used in the modified Matlab script *DiskScattering_differentR.m*. The radius of the upper disk is 5 μm and for the lower disk 10 μm .

Figure 3.18 shows the integral over the absolute square of the wave function for wavenumbers in the interval 550 to 1400 cm^{-1} for the system. As for the previous, section the wave function plots shown in the insets correspond to maxima in the integral. Also for the system with disks of different sizes a coupling between the resonances in the disks can be observed. The incoming plan wave is coming from the top of the system.

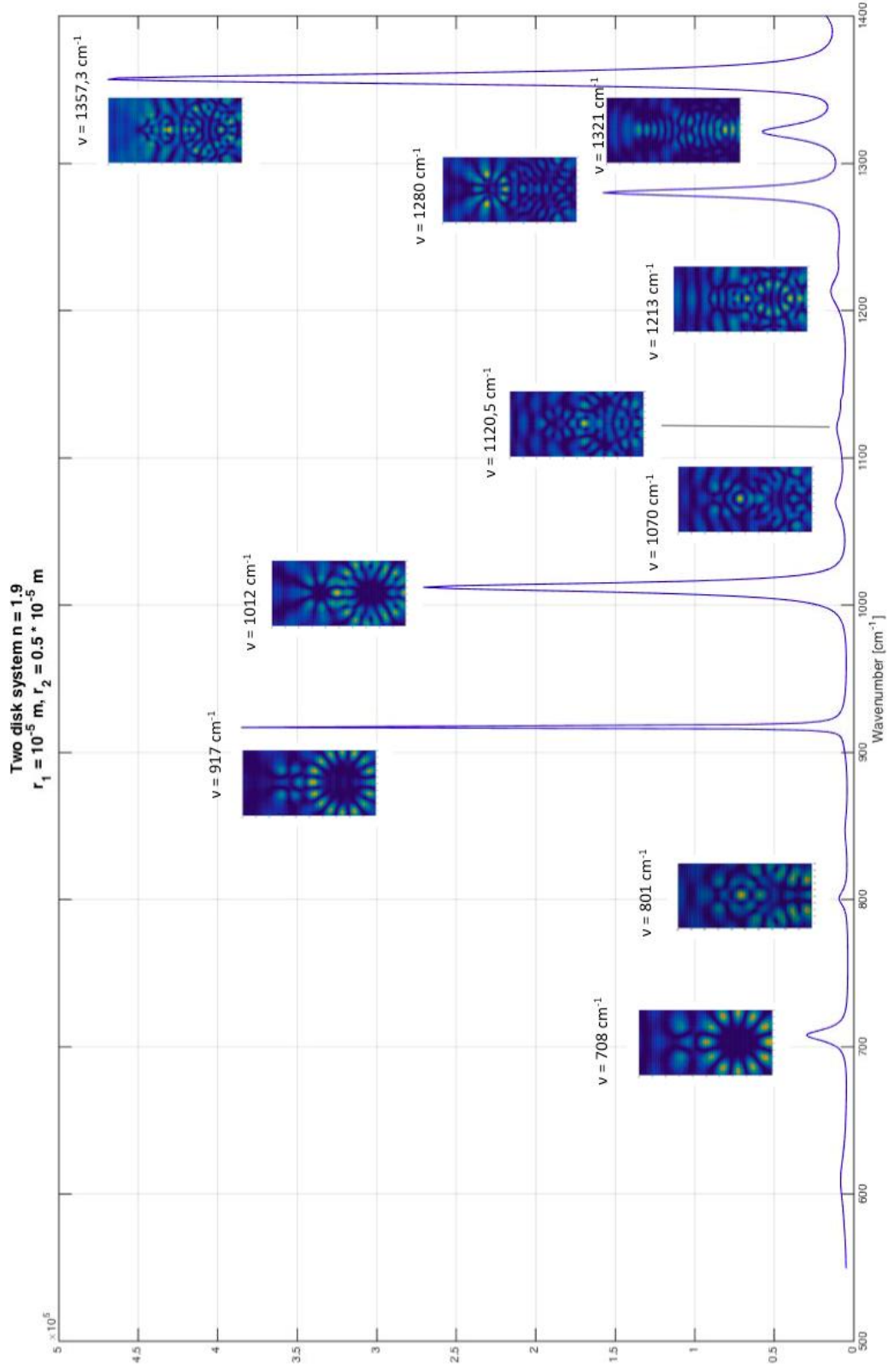


Figure 3.18 The integral over the absolute square of the wave function $|\bar{\Psi}|^2$ as a function of the wavenumber for a three-disk system with a refractive index equal $n = 1.9$. For each peak the absolute square of the wave function $|\bar{\psi}_j|^2$ is plotted. The radius of the upper disk is $5 \mu\text{m}$ and of the bottom disk is $10 \mu\text{m}$.

3.6 Plane-wave scattering in one-disk systems

To investigate if the whispering gallery modes in the two-disk system with different radii (Fig. 3.18), e.g. at $\nu = 917 \text{ cm}^{-1}$ and $\nu = 1012 \text{ cm}^{-1}$, have a connection with whispering gallery modes that occur in single-disk system, two different single-disk systems with different radii ($10 \text{ }\mu\text{m}$ and $5 \text{ }\mu\text{m}$) have been investigated. As refractive index we chose $n = 1.9$ for both of the systems. The graph of the integral over the absolute square of the wave function for wavenumbers in the interval 550 cm^{-1} to 1400 cm^{-1} for the single-disk systems is plotted in Figs 3.19-3.21. As previously, the insets show the wave functions that correspond to peaks in the graph of the integral. In Fig. 3.19 and Fig. 3.20 the radius of the disk is $10 \text{ }\mu\text{m}$, in Fig. 3.21 the radius of the disk is $5 \text{ }\mu\text{m}$. The incoming plan wave is coming from the top of the systems.

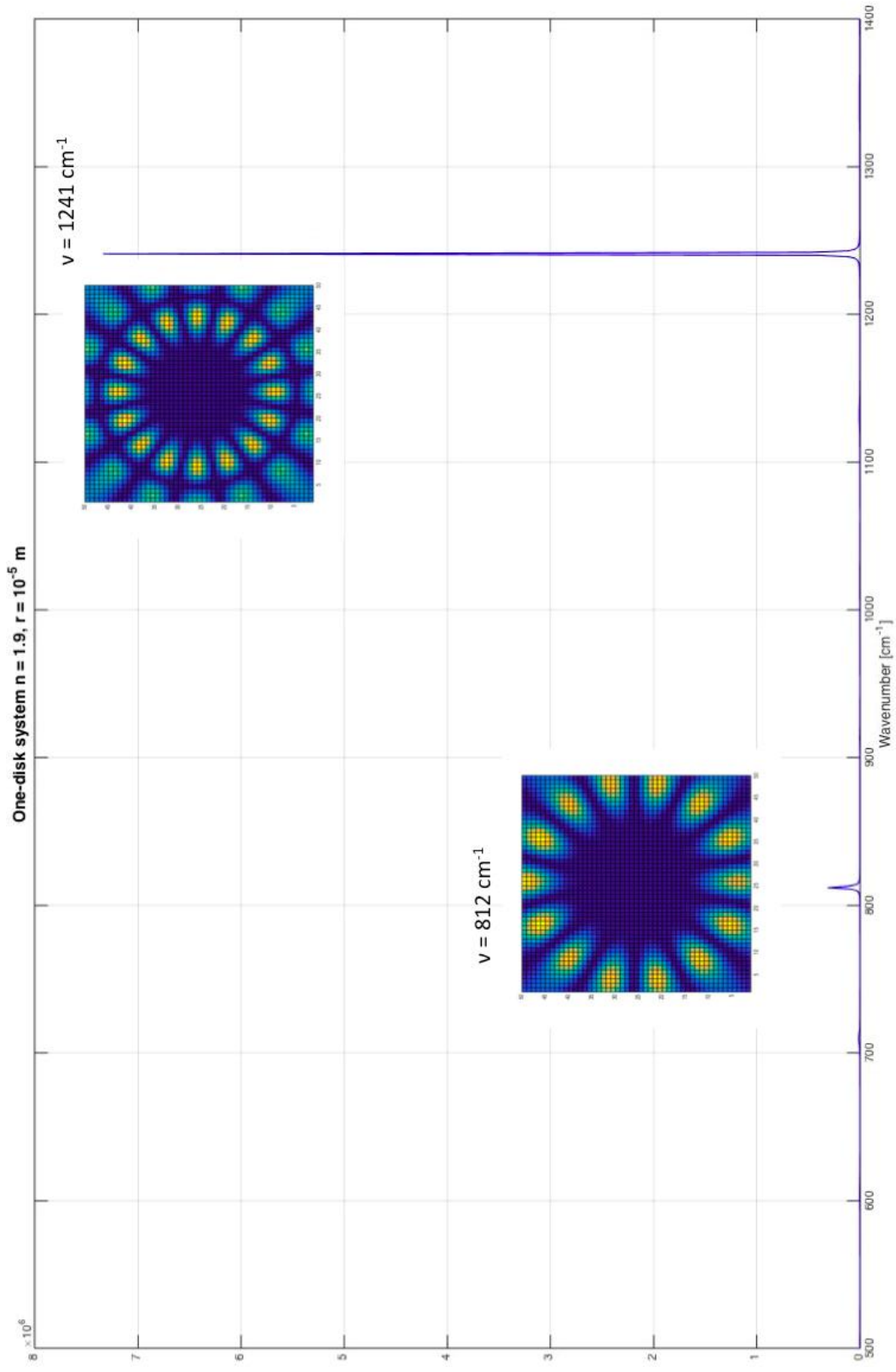


Figure 3.19 The integral over the absolute square of the wave function $|\bar{\Psi}|^2$ as a function of the wavenumber for one-disk system with a refractive index equal $n=1.9$. For each peak the absolute square of the wave function $|\bar{\psi}_j|^2$ is plotted. The radius of the disk is $10 \text{ }\mu\text{m}$.

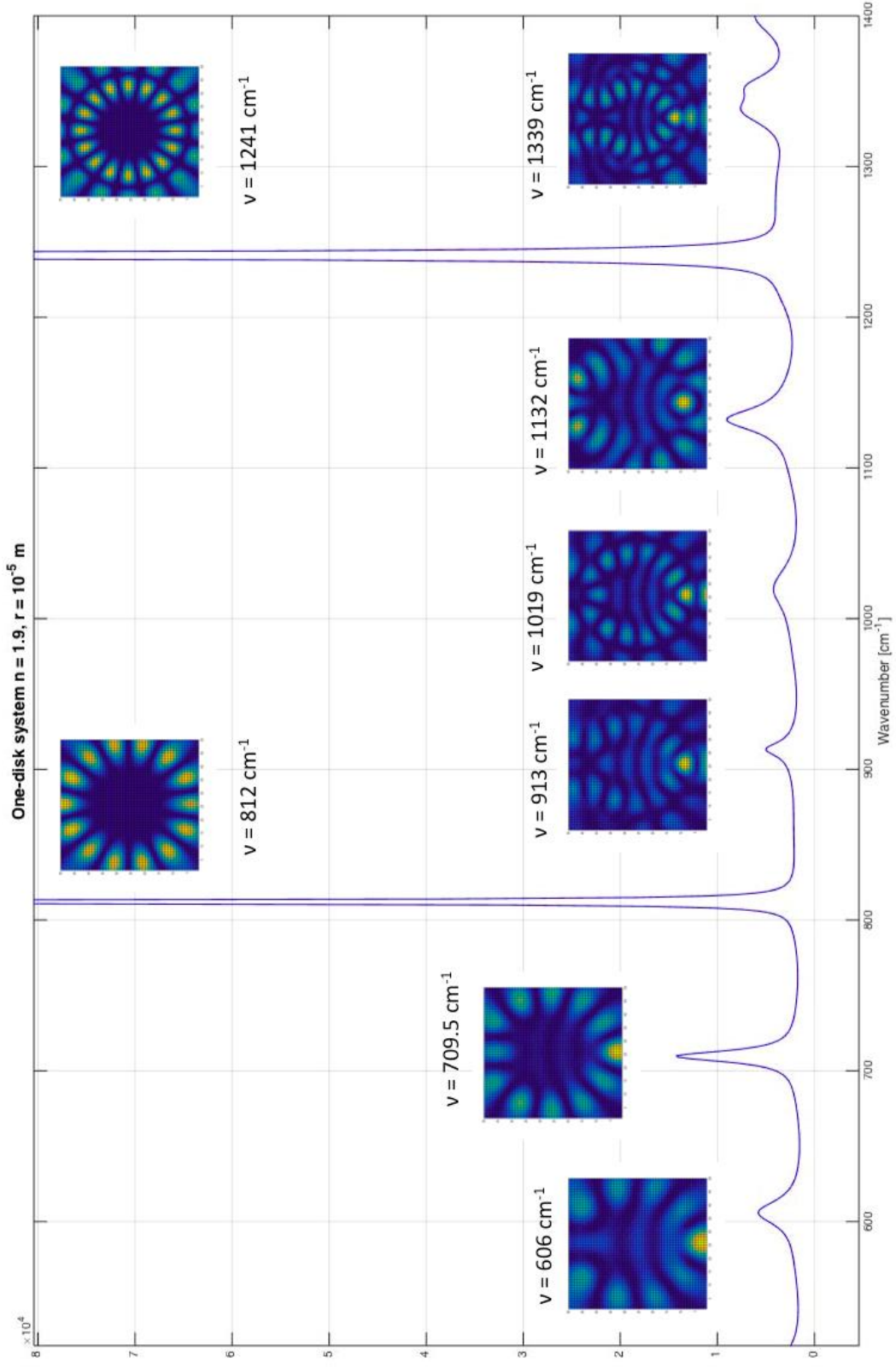


Figure 3.20 The integral over the absolute square of the wave function $|\Psi|^2$ as a function of the wavenumber for one-disk system with a refractive index equal $n=1.9$. For each peak the absolute square of the wave function $|\psi_j|^2$ is plotted. The radius of the disk is $10 \mu\text{m}$.

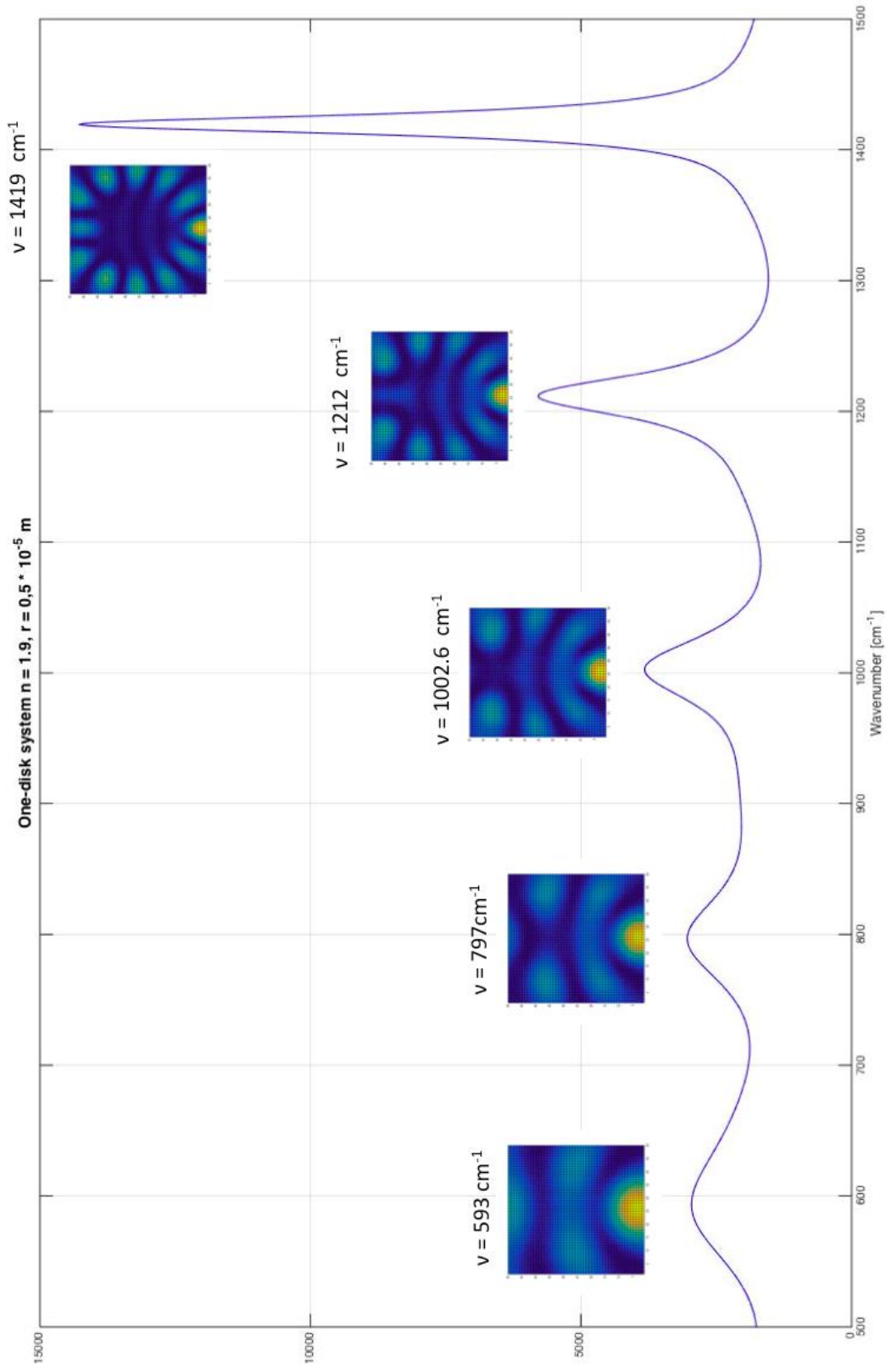


Figure 3.21 The integral over the absolute square of the wave function $|\Psi|^2$ as a function of the wavenumber for one-disk system with a refractive index equal $n=1.9$. For each peak the absolute square of the wave function $|\psi_j|^2$ is plotted. The radius of the disk is $5 \mu\text{m}$.

We further wanted to study if for the two whispering gallery modes that are present in the wave function plots in Fig. 3.18 at $\nu = 917 \text{ cm}^{-1}$ and $\nu = 1012 \text{ cm}^{-1}$, corresponding whispering gallery modes can be found in the respective single-disk systems. Wave function plots of wave functions at $\nu = 917 \text{ cm}^{-1}$ and $\nu = 1012 \text{ cm}^{-1}$ for the single-disk systems are represented in Fig. 3.22 and 3.12.

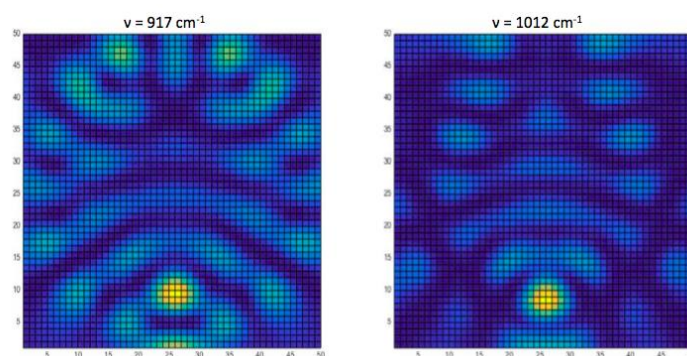


Figure 3.22 The square of the absolute value of the wave function for a single-disk system with radius $10 \mu\text{m}$ for wavenumber 917 cm^{-1} and 1012 cm^{-1} . The refractive index is 1.9

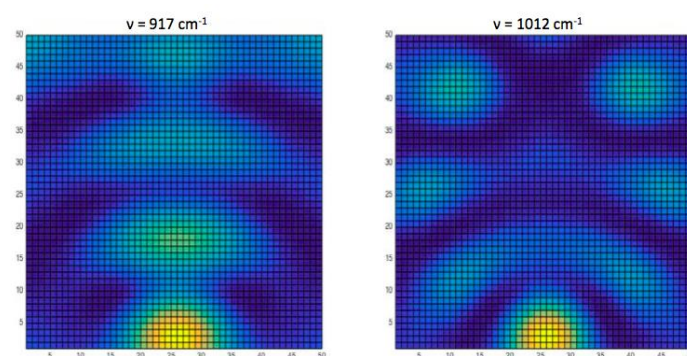


Figure 3.23 The square of the absolute value of the wave function for a single-disk system with radius $5 \mu\text{m}$ for wavenumber 917 cm^{-1} and 1012 cm^{-1} . The refractive index is 1.9.

It is obvious that the wave functions in the single-disk systems do not display whispering gallery modes at the same wave numbers as the corresponding two-disk system with radii $10 \mu\text{m}$ and $5 \mu\text{m}$. The positions of the whispering gallery modes seem to be shifted due to the coupling of the disks. This is expected when the coupling is strong. The whispering gallery mode at $\nu = 708 \text{ cm}^{-1}$ in Fig. 3.18 shows a rather weak coupling. The plot of the wave function shows a strong whispering gallery mode in the large disk, while the intensities in the small disk are rather weak. When inspecting the graph of the integral over the absolute square of the wave function of the single disks, we see that the respective peak in the integral is insignificantly for the largest disk. For the larger disk we find the corresponding whispering gallery mode at $\nu = 709.5 \text{ cm}^{-1}$ in Fig. 3.20.

3.7 Effect of the direction of the incoming plane wave on resonances in the two-disk system

For all examples we considered so far, the incoming plane wave was coming from the top of the disk systems. In order to investigate the stability of the plane-wave scatter algorithm, we investigated if a change in the direction of the incoming wave changes the position of the peaks in the graphs of the integrals of the absolute value of the wave functions. In Fig. 3.24 and 3.25, the plane wave is coming from the right of the two-disk system in leftward direction. As refractive index we chose 2.0 and the disks have equal radius. As previously, we plot the graph of the integrals of the absolute value of the wave functions in the interval 550 to 1400 cm^{-1} in the figures. The insets correspond to the resonant modes at the peak positions of the graph of the integral

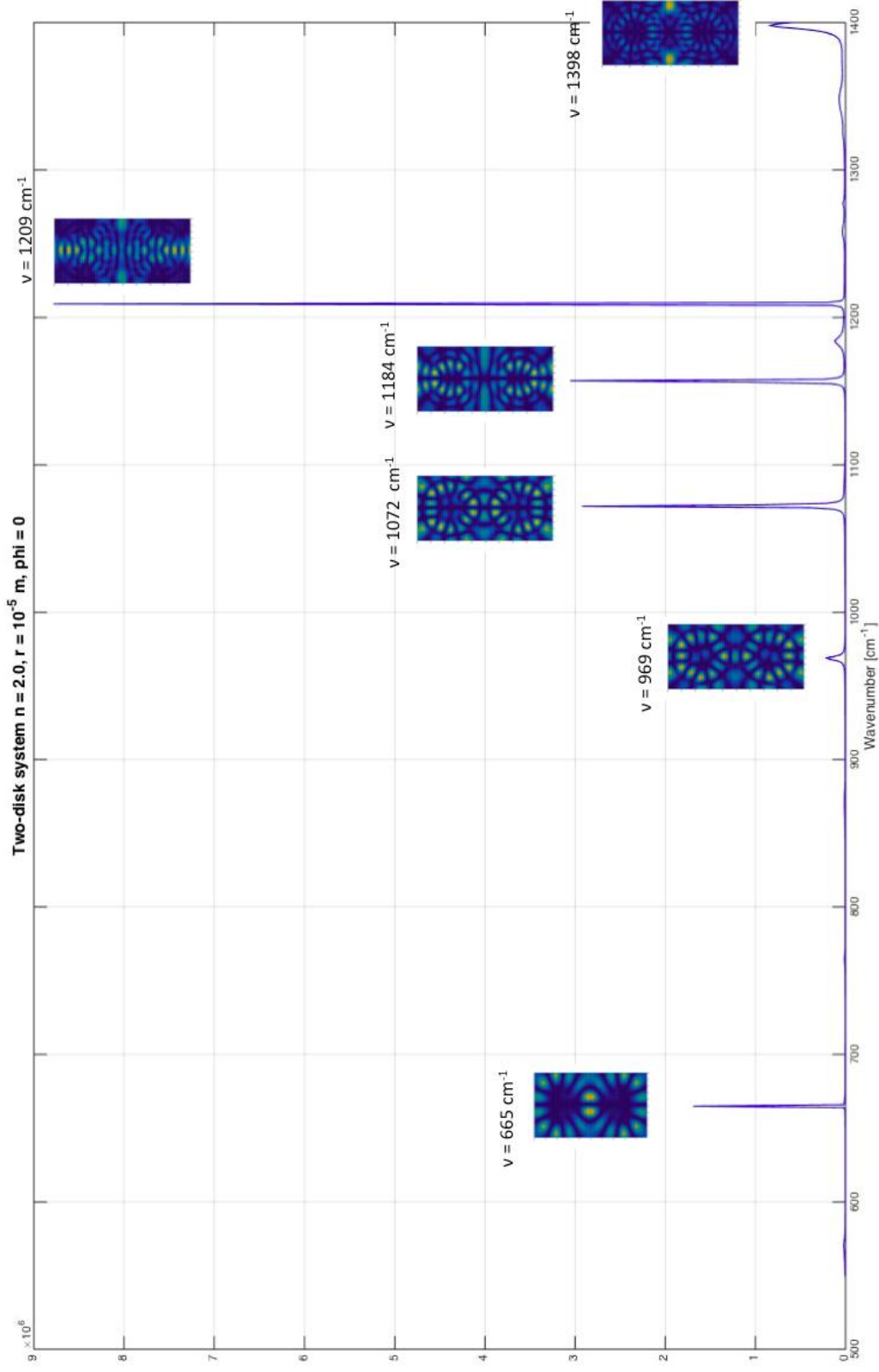


Figure 3.24 The integral over the absolute square of the wave function $|\Psi|^2$ as a function of the wavenumber for a two-disk system with a refractive index equal $n=2.1$. For each peak the absolute square of the wave function $|\vec{\psi}_j|^2$ is plotted. The radius of each disk is $10 \mu\text{m}$. The incoming wave is coming from the right.

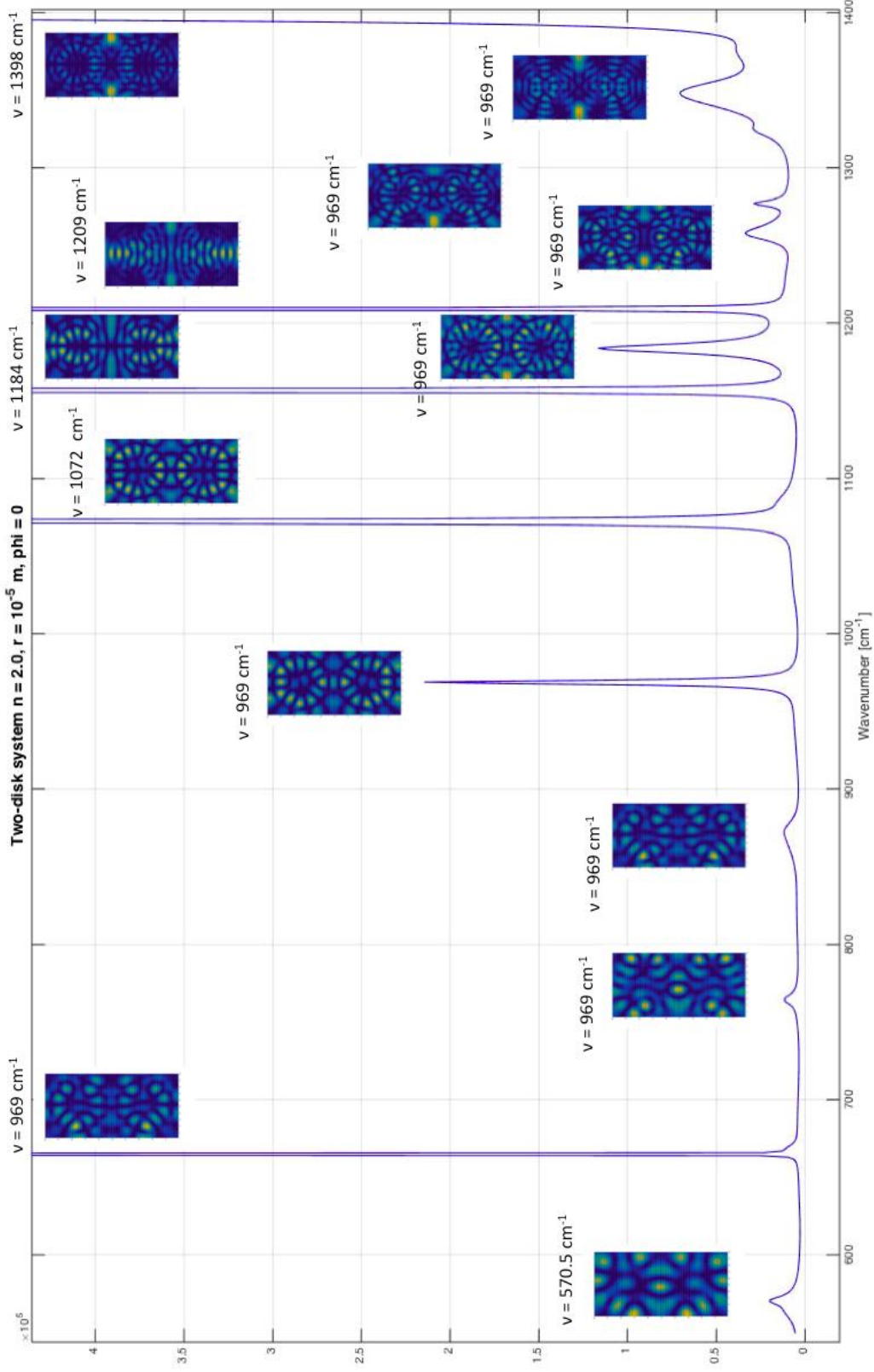


Figure 3.25 The integral over the absolute square of the wave function $|\bar{\Psi}|^2$ as a function of the wavenumber for a two-disk system with a refractive index equal $n=2.1$. For each peak the absolute square of the wave function $|\bar{\psi}_j|^2$ is plotted. The radius of each disk is $10 \mu\text{m}$. The incoming wave is coming from the right.

In the table 3.3 and table 3.4, the resonances for the incoming plane wave from the top in Fig. 3.12 and Fig. 3.13 are compared with the resonances for the incoming plane wave from the right in Fig. 3.24 and Fig. 3.25. It can be seen that the resonances appear at nearly the same wavenumbers.

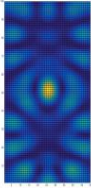
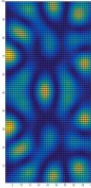
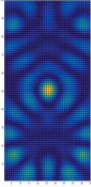
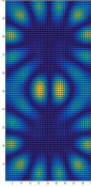
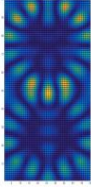
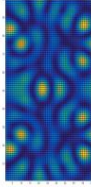
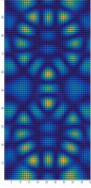
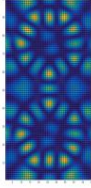
Incoming plane wave from the top	Incoming plane wave from the right
$\nu = 570.5 \text{ cm}^{-1}$ 	$\nu = 570.5 \text{ cm}^{-1}$ 
$\nu = 668 \text{ cm}^{-1}$ 	$\nu = 665 \text{ cm}^{-1}$ 
$\nu = 763 \text{ cm}^{-1}$ 	$\nu = 764 \text{ cm}^{-1}$ 
$\nu = 969 \text{ cm}^{-1}$ 	$\nu = 969 \text{ cm}^{-1}$ 

Table 3.3 Comparison of the resonances in a two-disk system with different direction of the incoming plane wave. The refractive index of the disks in both systems is 2.0.

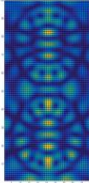
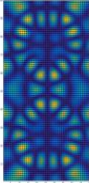
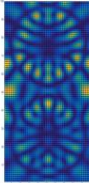
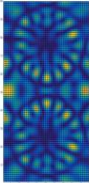
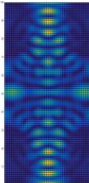
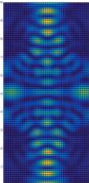
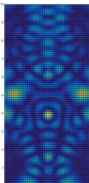
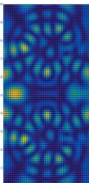
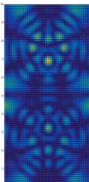
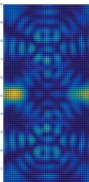
Incoming plane wave from the top	Incoming plane wave from the right
$\nu = 1080 \text{ cm}^{-1}$ 	$\nu = 1072 \text{ cm}^{-1}$ 
$\nu = 1183.5 \text{ cm}^{-1}$ 	$\nu = 1184 \text{ cm}^{-1}$ 
$\nu = 1209 \text{ cm}^{-1}$ 	$\nu = 1209 \text{ cm}^{-1}$ 
$\nu = 1256.5 \text{ cm}^{-1}$ 	$\nu = 1258 \text{ cm}^{-1}$ 
$\nu = 1343 \text{ cm}^{-1}$ 	$\nu = 1348 \text{ cm}^{-1}$ 

Table 3.4 Comparison of the resonances in a two-disk system with different direction of the incoming plane wave. The refractive index of the disks in both systems is 2.0.

Chapter 4

Discussion

The selection rule for the ray dynamics presented in chapter 2, has clear implications for the phase space of the ray dynamics. The selection rule leads to attractors, when the ratio between the refractive indices of the disks and the area around the disks is 1.78 or higher. From Fig. 2.5 and Fig. 2.6 it can be clearly seen, that the attractors have fractal structures. Due to the ray dynamics with a deterministic selection rule, the two-disk system goes from a chaotic phase space into a phase space with fractal attractors when the refractive index increases. For the parameters applied in this thesis, this transition occurs, when the refractive ratio equals 1.78. According to Ryu and Hentschel²⁵, the appearance of attractors is due to the ray model with a deterministic selection rule. Each ray that is started with a momentum $p = \pm 1/n$ has to stay in the system according to the ray model with a deterministic selection rule. Thus, all rays started within the momentum range $p = \pm 1/n$ represent the basin of attraction²⁵. A ray that is started within the momentum range $p = \pm 1/n$ approaches the attractor after some time. Since no ray can leave the system, any ray that is started close to an attractor can never leave the attractor²⁵. Similar phase space behavior as for the two-disk system could be observed for systems with more than two disks, when the ray model with a deterministic selection rule was employed. For systems with more than two disks, the placement of the Poincare surface of section not as obvious as for the two-disk system.

For solving the plane wave scattering problem different methods can be found in literature. For example the Maxwell equations can be solved by the finite difference time domain (FDTD) technique¹⁹. The FDTD technique is very time consuming and the stability of the technique is depending strongly on the geometry of the scatterers^{3, 18}. Other common solutions are based on partial wave equations²¹. Solutions based on partial wave equations are also prone to stability problems^{3, 18}. The methods evaluated in this

thesis are based on the discretization of the Lippmann-Schwinger equation. It shows surprisingly high stability given the simplicity of the solutions. The method could be used to produce the stable wave function results for different two-dimensional multiple-disk arrangements. The system program allows easily to change the direction of the incoming plane wave and differences in the wave function as a function of the incoming wave could be studied. It turned out that the position of the peaks in the integral over the square of the absolute value of the wave function did not depend on the direction of the incoming wave, which gave another proof of the stability of the method.

The integral over the square of the absolute value of the wave function directly related to the light absorption by the disks and has thus relevance for understanding the effectiveness of architectures of nanoimprints on thin solar films. It is therefore interesting to compare the integral over the square of the absolute value of the wave function for different parameters. The graph of the integral over the square of the absolute value of the wave function changes according to changes in phase space of the two-disk systems. For the system in Fig. 3.7 ($n = 1.7$, i.e. chaotic phase space according to the experiences in this thesis), the maximum value the integral is close to 4×10^4 . For the systems in Fig. 3.8-14 ($n \geq 1.8$, i.e. a phase space with attractors), the maximum value of the integral is between 2×10^6 and 10^8 . This could indicate that a higher coupling is present in systems in which the phase space contains strong attractors. When evaluating the integral over the square of the absolute value of the wave function for a three-disk system with a refractive index of $n=1.7$, the maximum value of the integral was 3×10^5 , which is higher than for the corresponding two-disk system. This may indicate that the higher number of disks leads to higher absorption and thus a higher efficiency in corresponding thin solar films with nanoimprints.

The maximum value of the integral over the squared absolute value of the wave function changes when the direction of the incoming plane wave changes. For a two-disk system with refractive index 2.0 and an incoming ray from the top, the maximum value of the integral is 10^8 . For a two-disk system with refractive index 2.0 and an incoming ray from the right is 9×10^6 . For two-disks systems with refractive index higher than 1.8 with an incoming plan wave from the top, a wave function is illustrated in Fig. 3.15. This particular wave function in Fig. 3.15 was with the two-disk central ray shown in Fig. 2.12 according to the quantization rule of Eq. 3-2 (see table 3.1). For a two-disk system with an incoming plane wave from right (section 3.7) this wave function did not occur. This fact may be interpreted with the help of ray dynamics. A ray entering the system from the right hand side, is not able to approach the attractor Fig. 2.12, since its momentum is zero in the x -direction.

The whispering gallery modes in the two-disk system (Fig. 3.4 and Fig. 3.5) are summarized in table 3.2. It is possible to follow the same whispering gallery mode type for different wavenumbers as the refractive index changes. This may allow in future to relate whispering gallery modes to strange attractor by the help of the quantization rule of Eq. 3-2.

For a two-disk system with refractive index 1.9 a whispering gallery mode with 14 maxima appeared at $\nu = 798 \text{ cm}^{-1}$ (Fig. 3.9). When this whispering gallery mode was compared with the corresponding whispering gallery mode in the one-disk system with radius $10 \text{ }\mu\text{m}$ (Fig. 3.19), the corresponding whispering gallery mode with 14 maxima was observed at $\nu = 812 \text{ cm}^{-1}$. Thus, it could be clearly seen that the coupling between the two disks leads to a shift in wavelength for the resonance.

When evaluating three-disk systems, similar resonances could be observed. Figure 3.16 illustrates examples of such resonances in three-disks systems. The coupling between the disks is obvious. The resonances for systems with three or more disks or with disks in a lattice structure will be an interesting subject for future investigations. Visually, the plane-wave scattering program reveals meaningful plots of wave functions also for three disk systems.

The plane-wave scattering program was further used to study two disks with different radii. Whispering gallery modes that appear in two-disk systems with different disk radii (Fig. 3.18) could be connected to the corresponding one-disk whispering gallery modes. As for the two-disk systems with equal radii of the disks, a shift in the wavenumber could be observed due to the coupling. The coupling of resonances in the two-disk system with different radii is nicely illustrated in Fig. 3.18.

For all calculations of the wave function in chapter 3, the distance between the disks was kept zero. When investigating the ray dynamics according to the ray model with a deterministic selection rule, two-disk systems with different distances between the disks were investigated. The ray dynamics shows clear changes, when the distance of the disks varies (Fig. 2.15). For two-disk systems with a distance zero and a refractive index of 2.0 (see Fig. 2.16 and Fig. 2.17) the phase space consists of a smaller number of stable islands, i.e. fewer attractors. According to Ryu and Hentschel²⁵ there is a shift in type of resonance as the distance between the disks changes. The strange attractors shown in Fig. 2.11 do not exist when the distance between the disks is zero. The strange attractors in Fig. 2.11 are reminiscent of lens²⁷. They collapse to the central attractor ray, when the distance between the lenses becomes zero. A further investigation of plane-wave scattering at disks with different distances may reveal the implications of these changes in the

phase space of the ray dynamics for the absorption properties of thin film solar cells with nanoimprints.

An error source that could influence the results in the calculations of the wave functions for the different disk-systems may be that the disks are located in the boarder of the area where the potential is defined. To investigate this error, these systems should be compared with systems that have a “frame” of zero potential around the original system.

Materials used in solar cells are usually TiO_2 or SiO_2 ¹⁹. The refractive index of these materials in the infrared region is around 2.5 and 1.5 and shows dispersion¹², where a changing refractive index is assumed. By changing the radius of the disks, it should be possible to obtain other resonances of the systems for these materials.

Materials used in solar cells are usually TiO_2 or SiO_2 ¹⁹. The refractive index of these materials in the infrared region is around 2.5 and 1.5 and shows dispersion¹². By investigating different architectures of nanoimprints for these materials with ray dynamics and plane wave scattering algorithms it may in future be possible to perform targeted light management

Chapter 5

Conclusion and outlook

The aim of this thesis was to investigate to what extent the increased efficiency in thin film solar cells with spherical nanoimprints could be explained by a coupling of spheres. In order to study this subject in the frame of this thesis, it was decided to study the coupling in two-dimensional model systems, i.e. systems with two and more disks. Both the ray dynamics and the wave dynamics in these systems were investigated. For the ray dynamics, a deterministic selection rule was implemented. The ray model with a deterministic selection rule allowed studying the phase space. It was shown that a chaotic phase space could be obtained for low refractive indices. For higher refractive a phase space with strange attractors was obtained, i.e. the attractors showed fractal structures. A plane-wave scattering algorithm based on the Lippmann-Schwinger equation was evaluated for different disk systems. The plane wave-scattering algorithm turned out to be very stable. Its stability allowed following the appearance of specific whispering gallery mode types with increasing refractive index. The whispering gallery mode types appeared at specific wavenumbers and were subjected to systematic wavenumber shifts, when the refractive index of the respective system changed. The stability of the algorithm was further confirmed, when we studied incoming plane waves impinging on the disk systems from different directions. The positions of the whispering gallery modes in the wavenumber space were nearly independent on the direction of the incoming plane wave. A comparison of the ray dynamics with the plane wave scattering results, revealed clear connections. When the phase space of the ray dynamics with a deterministic selection rule changed from a chaotic phase space to a phase space with strange attractors, a clear change in the intensity of the integral over the square of the absolute value of the wave function could be seen. Future investigations are necessary to investigate how this knowledge over the changes in the phase space behavior and its implications for the wave dynamics can be utilized for thin film solar cells with nanoimprints. Several of the coupled

mode types that were observed when investigating the wave dynamics could be directly related to the strange attractors by a quantization rule. This shows that the ray dynamics can potentially be used to understand and to optimize architectures of nanoimprints. Further research is necessary, in order to understand how the knowledge about the relevance of strange attractors for absorption properties can be exploited for solar cells with nanoimprints. The wave functions of the multiple-disk system presented in this thesis, gave further indications that a coupling between the disks influences the absorption significantly. This seems to be valid for disk-systems with both equally and differently sized disks.

In summary, we can conclude that the coupling of disks is important for the absorption properties of nanoimprints in thin film solar cells. The study of the ray dynamics with a deterministic selection rule in coupled systems revealed a deeper understanding of the significance of the coupling for the enhancement of absorption properties.

Bibliography

1. Berry, M. V. (1981). Regularity and chaos in classical mechanics, illustrated by three deformations of a circular 'billiard'. *Eur. J. Phys*, 2 (2): 91-102.
2. Blümel, R., Antonsen, J. T. M., Georgeot, B., Ott, E. & Prange, R. E. (1996). Ray Splitting and Quantum Chaos. *Physical Review Letters*, 76 (14): 2476-2479.
3. Blümel, R. (2015). rblumel@wesleyan.edu.
4. Boyle, G. (2012). *Renewable energy : power for a sustainable future*. 3rd ed. ed. Oxford: Oxford University Press/The Open University.
5. Couchman, L., Ott, E. & Antonsen, T. M. (1992). Quantum chaos in systems with ray splitting. *Physical Review A*, 46 (10): 6193-6210.
6. *DiskScattering_20082015.m* (2015). The program was developed by Kohler, A. and Blümel, R. To investigate two-disk system with different radii, the program was modified by Brandsrud, M.A. (*Disk_Scattering_differentR.m*). The codes are given in the appendix. .
7. Grandidier, J., Callahan, D. M., Munday, J. N. & Atwater, H. A. (2011). Light Absorption Enhancement in Thin - Film Solar Cells Using Whispering Gallery Modes in Dielectric Nanospheres. *Advanced Materials*, 23 (10): 1272-1276.
8. Grandidier, J., Weitekamp, R. A., Deceglie, M. G., Callahan, D. M., Battaglia, C., Bukowsky, C. R., Ballif, C., Grubbs, R. H. & Atwater, H. A. (2013). Solar cell efficiency enhancement via light trapping in printable resonant dielectric nanosphere arrays. *physica status solidi (a)*, 210 (2): 255-260.
9. Hlushchuk, Y., Kohler, A., Bauch, S., Sirko, L., Blümel, R., Barth, M. & Stöckmann, H.-J. (2000). Autocorrelation function of level velocities for ray-splitting billiards. *Physical Review E*, 61 (1): 366.
10. Hulst, H. C. v. d. (1981). *Light scattering by small particles*. New York: Dover.
11. Johan F. Aarnes, Ø. G. (2014, December 27). *Fraktal: fysikk, matematikk*. Store norske leksikon. Available at: [https://snl.no/fraktal%2Ffysikk%2C matematikk](https://snl.no/fraktal%2Ffysikk%2C%20matematikk). (accessed: 2015, December 12).

12. Kischkat, J., Peters, S., Gruska, B., Semtsiv, M., Chashnikova, M., Klinkmüller, M., Fedosenko, O., Machulik, S., Aleksandrova, A., Monastyrskiy, G., et al. (2012). Mid-infrared optical properties of thin films of aluminum oxide, titanium dioxide, silicon dioxide, aluminum nitride, and silicon nitride. *Applied Optics*, 51 (28): 6789-6798.
13. Kohler, A., Killesreiter, G. & Blümel, R. (1997). Ray splitting in a class of chaotic triangular step billiards. *Physical Review E*, 56 (3): 2691.
14. Kohler, A. & Blümel, R. (1998). Annular ray-splitting billiard. *Physics Letters A*, 238: 271-277.
15. Kohler, A. & Blümel, R. (1998). Signature of periodic lateral-ray orbits in a rectangular ray-splitting billiard. *Physics Letters A*, 247 (1): 87-92.
16. Kohler, A. & Blümel, R. (1998). Weyl formulas for quantum ray-splitting billiards. *Annals of Physics*, 267 (2): 249-280.
17. Kohler, A. & Blümel, R. (1999). Test of semiclassical amplitudes for quantum ray-splitting systems. *Physical Review E*, 59 (6): 7228.
18. Kohler, A. (2015). achim.kohler@nmbu.no.
19. Lukacs, R. (2015). rozalia.lukacs@nmbu.no.
20. Mark, L. B., Yi, C. & Shanhui, F. (2014). Light management for photovoltaics using high-index nanostructures. *Nature Materials*, 13 (5): 451.
21. Newton, R. G. (1966). *Scattering Theory of Waves and Particles*. New York: McGraw-Hill Book Company.
22. Paul A. Tipler, G. M. (2008). *Physics for scientists and engineers*. 6 ed. New York, USA: W.H. Freeman and Company.
23. Paul, S. & Ray, M. (2013). Periodically repeated gap-independent transmission in waveguide coupled microring Whispering Gallery Resonators (WGR). *Journal of Optics*, 42 (3): 203-207.
24. *plot_ray.m and PSOS.m complete with functions*. (2015). Developed by Brandsrud, M. A. The codes are given in the appendix. .
25. Ryu, J.-W. & Hentschel, M. (2010). Ray model and ray-wave correspondence in coupled optical microdisks. *Physical Review A*, 82 (3): 1-8.
26. Savytskyy, N., Kohler, A., Bauch, S., Blümel, R. & Sirko, L. (2001). Parametric correlations of the energy levels of ray-splitting billiards. *Physical Review E*, 64 (3): 036211.

27. Tipler, P. A. & Mosca, G. (2008). *Physics for scientists and engineers : with modern physics*. 6th ed. ed. New York: Freeman.
28. UNINETT Sigma2 AS. *Stallo* - *Sigma2*. Available at: <https://www.sigma2.no/content/stallo> (accessed: 13.12.15).
29. Weisstein, E. W. *Attractor*. From MathWorld - A Wolfram Web Resource. <http://mathworld.wolfram.com/Attractor.html> (accessed: 12.12.15).
30. Weisstein, E. W. *Basin of Attraction*. From MathWorld--A Wolfram Web Resource. Available at: <http://mathworld.wolfram.com/BasinofAttraction.html> (accessed: 12.12.15).
31. Yao, Y., Yao, J., Narasimhan, V. K., Ruan, Z., Xie, C., Fan, S. & Cui, Y. (2012). Broadband light management using low-Q whispering gallery modes in spherical nanoshells. *Nature communications*, 3: 664.

Appendix

In this appendix Matlab codes is given. The scripts²⁴ that is used in chapter 2 is:

- *plot_ray.m*
Plots the pattern a ray will follow in a disk system with the deterministic selection rule.
- *PSOS.m*
Plots the phase space for a
- *disk.m* (function)
Gives the positions for transmission/refraction for *plot_ray.m*
Gives the p and s for *PSOS.m*
- *test_hit.m* (function)
Check if the ray will hit the other disk or not (selection rule)
- *new_values.m* (function)
Calculates the point where the disk will hit the new disk

For calculations of the wave function *Disk_Scattering20082015.m*⁶ in chapter 3. To calculate the wave function for a system with different radius of the two disks, this code was modified to *Disk_Scattering_differentR.m*⁶.

```

%%%%%%%%%%%%%%%%%%%%%%%%%%%%%%%%%%%%%%%%%%%%%%%%%%%%%%%%%%%%%%%%%%%%%%%%
% plot_ray.m
%
% Plot a ray in a disk-system with the deterministic selection rule
% found by Ryu and Hentschel.
%
% The disks if established in a line of disks, 1 x n disks.
%
% The rays start in the upper half of one of the disks.
%
%%%%%%%%%%%%%%%%%%%%%%%%%%%%%%%%%%%%%%%%%%%%%%%%%%%%%%%%%%%%%%%%%%%%%%%%
close all

%% INPUT
no_of_disks = 2;           % The total number of disks
n1 = 1.0;                 % The refractive index of the medium around the
                           % disks
n2 = 1.9;                 % The refractive index of the disks
no_of_bounces = 300;     % The total number of transmissions/reflections
r = 1.0;                  % The radius of the disks
start_disk = 1;          % The disk the rays starts from
disk_no_PSOS = 1;        % The disk where the phase space is found. Not used
                           % in this plot.
start = 25;               % The transmission/reflection where the plotting
                           % starts.
d = r;                    % The distance between the disks (distance between
                           % to center points = d + 2*r)

%% Start conditions:
s0 = 0.5;
p0 = 0.3;

%% Plotting the disk system:
xs = 0;
ys = 0;
ang=0:0.0001:2*pi;
xp=r*cos(ang);
yp=r*sin(ang);

for i =1:no_of_disks
    plot((xp+(i-1)*(2*r+d)), (yp), 'r');
    axis( [-1.5*r] ((no_of_disks-1)*(d+2*r)+1.5*r) [-1.5*r] (1.5*r));
    grid on
    hold on
end

%% Plotting the rays behavior into the disk system:
[z, s, p] = disks(s0, p0, no_of_disks, n1, n2, no_of_bounces, r, start_disk,
disk_no_PSOS, start, d);
for n = start:no_of_bounces
    plot([real(z(n-1)) real(z(n))], [imag(z(n-1)) imag(z(n))], 'b');
end

```

```

%%%%%%%%%%%%%%%%%%%%%%%%%%%%%%%%%%%%%%%%%%%%%%%%%%%%%%%%%%%%%%%%%%%%%%%%
% PSOS.m
%
% Finding the phase space for a disk system in terms of the Poincarè
% surface of section (PSOS).
%
%%%%%%%%%%%%%%%%%%%%%%%%%%%%%%%%%%%%%%%%%%%%%%%%%%%%%%%%%%%%%%%%%%%%%%%%

clear all

%% INPUT
no_of_disks = 2;           % The total number of disks
n1 = 1.0;                 % The refractive index of the medium around the
                           % disks
n2 = 1.9;                 % The refractive index of the disks
no_of_bounces = 300;     % The total number of transmissions/reflections
r = 1.0;                  % The radius of the disks
start_disk = 1;          % The disk the rays starts from
disk_no_PSOS = 1;        % The disk where the phase space is found. Not used
                           % in this plot.
start = 25;               % The transmission/reflection where the plotting
                           % starts.
d = r;                    % The distance between the disks (distance between
                           % to center points = d + 2*r)
n = 10;                   % The total number of attractors in the PSOS

%% Random generation of p, x0 and alpha

close all
s0 = [];
p0 = [];
s = zeros(n,1);
p = zeros(n,1);
z = zeros(n,1);

% Generation of random start points
for b = 1:n;
    rng = ('shuffle');
    random_s0 = rand;
    random_p0 = rand;
    p0(b) = random_p0*(n1/n2)*2 - (n1/n2) ;    % p = sin(theta2)
    s0(b) = random_s0;                        % S/Smax
end

%% Make s-matrix and p-matrix (and z-matrix)
for k = 1:n
    [z_array, s_array, p_array] = disks(s0(k), p0(k), no_of_disks, n1, n2,
no_of_bounces, r, start_disk, disk_no_PSOS,start,d) ;
    for j = 1:length(s_array)
        s(k,j) = s_array(j);
        p(k,j) = p_array(j);
    end

    % The z-array can be saved and plotted for investigations of the

```

```
    % different attractors the rays stabilize into
    %   for g = 1:length(z_array)
    %       z(k,g) = z_array(g);
    %   end
end

%% Plot of the PSOS
for k = 1:n
    for l = 1:length(s(k,:));
        if s(k,l) == 0
            else
                plot(s(k,l), p(k,l) , 'b. ');
                grid on
                hold on
            end
        end
    end
end
```

```

%%%%%%%%%%%%%%%%%%%%%%%%%%%%%%%%%%%%%%%%%%%%%%%%%%%%%%%%%%%%%%%%%%%%%%%%
% disk.m
%
% Find the path the ray will follow. Put it together in a vector
%
%%%%%%%%%%%%%%%%%%%%%%%%%%%%%%%%%%%%%%%%%%%%%%%%%%%%%%%%%%%%%%%%%%%%%%%%

function [z, s, p] = disks(s0, p0, no_of_disks, n1, n2, no_of_bounces, r,
start_disk, disk_no_PSOS, start, d)

% Gives the behavior of the disk in

z = []; % The position (in complex numbers)
p = []; % The p-value of the selected disk (For plotting of PSOS)
s = []; % The s-value of the selected disk (For plotting of PSOS)
f = 0; % The length of the p and s vector
k = 1; % No bounces inside one disk
hit = 0; % Gives indications of transmission or reflection.

% In case of total reflection:
if abs(p0) > n1/n2
    error('p is too high');
end

for n = 1:no_of_bounces
    if n == 1 % The first point
        theta2 = asin(p0);
        theta1 = asin(sin(theta2)*n2/n1);

        if theta2 < 0 % The direction of rotation
            dir = 1; % counterclockwise
        else
            dir = -1; % clockwise
        end

        phi = pi - s0*r*pi; % The complex angle
        z(n) = r * exp(1i * phi) + (start_disk-1)*(d+2*r);
        disk_no = start_disk;

% When it is change of disk. Find point where the disk hits.
elseif disk_no == 0
    k = 1;
    hit = 0;
    [disk_no, z(n), phi, theta1, dir] = new_values(disk_no_old, z(n-1),
abs(theta1), dir, r, d);

% Calculations inside disk
else
    k = k + 1;
    theta2 = asin(sin(abs(theta1))*n1/n2) * (-dir); % if dir = -1,
theta2 > 0
    delta_phi = pi - 2*abs(theta2);
    point = r * exp(1i*(phi+dir*(k-1)*delta_phi));
    z(n) = point + (disk_no-1)*(d+2*r);
    ang = acos(real(point)/r);

```

```

% Deterministic selection rule
if disk_no == 1 && real(point) < 0
elseif disk_no == no_of_disks && real(point) > 0
else
    [hit] = test_hit(z(n), abs(theta1), d, r, dir, disk_no);
end
end

% Data to the PSOS
if disk_no == disk_no_PSOS && imag(z(n)) > 0 && n > start
    v = pi - angle(z(n) - (disk_no-1)*(d+2*r));
    f = f + 1;
    s(f) = v/pi;          %S/Smax
    theta2 = asin(sin(abs(theta1))*n1/n2) * (-dir);
    p(f) = sin(theta2); %p = sin(theta)
end

% In case of changing disk. Indicate a change of disk.
if hit == 1
    disk_no_old = disk_no;
    disk_no = 0; %between the disks.
end
end

```

```

%%%%%%%%%%%%%%%%%%%%%%%%%%%%%%%%%%%%%%%%%%%%%%%%%%%%%%%%%%%%%%%%%%%%%%%%
% hit.m
%
% Check if the ray will hit one of the other disks or not.
%
% No hit: hit = 0
% Hit: hit = 1
%
%%%%%%%%%%%%%%%%%%%%%%%%%%%%%%%%%%%%%%%%%%%%%%%%%%%%%%%%%%%%%%%%%%%%%%%%

function [hit] = test_hit(z, thetal, d, r, dir, disk_no)

h = [];
hit = 0;    % Sets hit to 0

x = real(z) - (2*r + d)*(disk_no-1);
y = imag(z);

%Transfer situation
if x < 0 %flip
    x = - x;
    dir = - dir;
end

if dir == -1
    y = - y;
    dir = -dir;
end

%% Finding angles of the ray
psi = acos(abs(x/r));
alpha = acos(abs(y/r));

%% Check of hit of not
if y < 0
    if (abs(thetal) + alpha) < pi/2

        phi = pi/2 - (thetal + alpha);

        ang = pi:0.0001:(3*pi/2); % The accuracy
        yp = r*sin(ang);
        xp = r*cos(ang);

        for n = 1:length(xp)
            if alpha < pi/4
                h(n) = ((d + (r-x) + (r-xp(n))) * tan(phi)) + abs(y);
            else
                h(n) = ((d + (r-x) + (r-xp(n))) / tan(pi/2 - phi)) +
abs(y);
            end

            if h(n) < abs(yp(n))
                hit = 1;
                return
            end
        end
    end
end

```



```

end

else
    phi = (alpha + theta1) - pi/2;

    ang = (pi/2):0.0001:(3*pi/2); % The accuracy
    yp = r*sin(ang);
    xp = r*cos(ang);

    for n = 1:length(xp)
        if phi < pi/4
            h(n) = ((d + (r-x) + (r-abs(xp(n)))) * tan(phi)) -
abs(y);
        else
            h(n) = ((d + (r-x) + (r-abs(xp(n)))) / tan(pi/2 - phi))-
abs(y);
        end

        if h(n) < 0
            hit = 1;
            return
        elseif h(n) <= yp(n)
            hit = 1;
            return
        end

    end

end

end

else
    phi = theta1 + psi;

    if (phi) > acos(r/((r-x)+r+d))
        return
    end

    ang = (pi/2):0.0001:pi;
    yp = r*sin(ang);
    xp = r*cos(ang);

    for n = 1:length(xp)
        if phi < pi/4
            h(n) = y + ((d + (r-x) + (r-abs(xp(n)))) * tan(phi));
        else
            h(n) = y + ((d + (r-x) + (r-abs(xp(n)))) / tan(pi/2 - phi));
        end

        if h(n) < yp(n)
            hit = 1;
            return
        end
    end

end

end

```

```

%%%%%%%%%%%%%%%%%%%%%%%%%%%%%%%%%%%%%%%%%%%%%%%%%%%%%%%%%%%%%%%%%%%%%%%%
% new_values.m
%
% Calculates the point where the ray will hit the next disk in case of
% transmission, i.e. hit = 1 in test_hit.m
%
%%%%%%%%%%%%%%%%%%%%%%%%%%%%%%%%%%%%%%%%%%%%%%%%%%%%%%%%%%%%%%%%%%%%%%%%

function [disk_no_new, z_new, phi_new, thetal_new, dir_new ] =
new_values(disk_no_old, z, thetal, dir, r,d)

% Transfer into a Cartesian coordinate system
x = real(z) - (2*r + d)*(disk_no_old-1);
y = imag(z);

% Angles in the system
psi = acos(abs(x/r));
alpha = acos(abs(y/r));
A = (d + 2*r) - abs(x);
dir_new = 0;
k = 1;

% Transfer situation, flip
if x < 0
    dir = -dir;
    x = -x; %all x-values > 0.
end

if y > 0
    if dir == -1
        if (alpha + thetal) > pi/2
            u = -1;
            ang = (alpha + thetal) - pi/2;
        else
            u = 1;
            ang = pi/2 - (alpha + thetal);
            dir_new = -1;
        end
    else %dir = 1
        ang = thetal + psi;
        u = 1;
        dir_new = -1;
    end
else % y < 0
    if dir == -1
        u = -1;
        ang = thetal + psi;
        dir_new = 1;
        k = -1;
    else %dir = 1
        if (alpha + thetal) > pi/2
            u = 1;
            ang = (alpha + thetal) - pi/2;
            k = -1;
        end
    end
end

```

```

        else
            u = -1;
            ang = pi/2 - (alpha + theta1);
            dir_new = 1;
            k = -1;
        end
    end
end

delta_x = min(roots([1 (u*2*cos(ang)*sin(ang)*y - 2*A*(cos(ang))^2) ((A^2 +
y^2 - r^2)*cos(ang)^2)]));

x_new = -(A-delta_x);

if ang < pi/4
    y_new = y + u*delta_x * tan(ang);
else
    y_new = y + u*delta_x / tan(pi/2 - ang);
end

if dir_new == 0
    alpha_new = acos(abs(x_new/r));
    if y > 0 && y_new < 0
        dir_new = 1;
        k = -1;
    elseif y < 0 && y_new > 0
        dir_new = -1;
        k = 1;
    elseif y > 0
        if alpha_new > ang
            dir_new = -1;
        else
            dir_new = 1;
        end
    else
        if alpha_new > ang
            dir_new = 1;
        else
            dir_new = -1;
        end
    end
end

thetal_new = acos(abs(x_new/r))+u*ang*k;

if thetal_new < 0
    thetal_new = -thetal_new;
    dir = -dir;
end

if real(z) - (2*r + d)*(disk_no_old-1) < 0
    disk_no_new = disk_no_old - 1;
    x_new = -x_new;
    dir_new = -dir_new;
else
    disk_no_new = disk_no_old + 1;
end

```

```
end

%% The point at the new disk
phi_new = angle(x_new + 1i*y_new);
z_new = x_new + 1i*y_new + (2*r + d)*(disk_no_new-1);
```

```

%%%%%%%%%%%%%%%%%%%%%%%%%%%%%%%%%%%%%%%%%%%%%%%%%%%%%%%%%%%%%%%%%%%%%%%%
% Disk_Scattering20082015.m
%
% Calculates the wave function for a two-dimensional system
%
%%%%%%%%%%%%%%%%%%%%%%%%%%%%%%%%%%%%%%%%%%%%%%%%%%%%%%%%%%%%%%%%%%%%%%%%

clear all;
close all;

ArrayOfCircles=1;

nu= 1323 * 100.0;    % The wavenumber nu (cm-1) * 100)
phi=pi/2.0;
k=2*pi*nu;
kx=k*cos(phi);
ky=k*sin(phi);
clear phi;

NCx=1;              % No of disks in x-direction
NCy=2;              % No of disks in y-direction

R=power(10,-5);    % Radius
Nx=50;              % Resolution in x-direction
Ny=100;             % Resolution in y-direction
N=Nx*Ny;
a=2*NCx*R;
b=2*NCy*R;
n_index=1.7;        % Refractive index of the disk(s)

dx=a/Nx; % spacing in x-direction
dy=b/Ny; % spacing in y-direction

x=zeros(1,N);
y=zeros(1,N);
for i=1:Nx
    for l=1:Ny

        j=(l-1)*Nx+i;
        x(j)=(i-0.5)*dx;
        y(j)=(l-0.5)*dy;

    end
end

G=zeros(N,N);

for j=1:N
    for m=1:N

        % H is not defined for zero argument
        if (j==m)
            G(j,m)=0.0;
        else

```

```

        Z=k*sqrt((x(j)-x(m))*(x(j)-x(m))+(y(j)-y(m))*(y(j)-y(m)));
        G(j,m)=besselh(0,Z);    %besselh(nu,Z) gives Hankel function
                                H_0^+
    end

end

end

% Establish the potential
v=zeros(1,N);
for m=1:N

    for nx=1:NCx
        for ny=1:NCy

            if (ArrayOfCircles)
                % Array of circles
                xcircle=(2*nx-1)*R;
                ycircle=(2*ny-1)*R;

                rn=sqrt((x(m)-xcircle)*(x(m)-xcircle)+(y(m)-ycircle)*(y(m)-
ycircle));
                if (rn<R)
                    v(m)=1.0-n_index*n_index;
                end
            end

        end

    end

end

Gtilde=zeros(N,N);

for j=1:N
    for m=1:N

        Gtilde(j,m)=G(j,m)*v(m);

    end

end

clear G;
clear v;

eikr=zeros(1,N);
for j=1:N
    eikr(j)=exp(1i*(kx*x(j)+ky*y(j)));
end
clear x y;

M=zeros(N,N);
IdentityMat=eye(N,N);
M=IdentityMat+1i*(k*k*dx*dy*0.25)*Gtilde;

```

```
clear Gtilde;
clear IdentityMat;

%% Solve Linear Equation by Matlab routine
psi_complex = linsolve(M,eikr');
psi_complex_reshaped=reshape(psi_complex,Nx,Ny);

Xplot=abs(psi_complex_reshaped).*abs(psi_complex_reshaped);

figure;
pcolor(Xplot');
set(gcf,'Color',[1 1 1]);

phi=zeros(Nx,Ny);
phi=angle(psi_complex_reshaped); % gives angles in the range -pi:pi

figure;
pcolor(phi');
set(gcf,'Color',[1 1 1]);

% Integrating over the absolute square of the wave function
linearIndexXplot=sub2ind(size(Xplot),Nx,Ny);
IntegralPsi=sum(Xplot(1:linearIndexXplot));
```

```

%%%%%%%%%%%%%%%%%%%%%%%%%%%%%%%%%%%%%%%%%%%%%%%%%%%%%%%%%%%%%%%%%%%%%%%%
% Disk_Scattering_differentR.m
%
% Calculates the wave function for a two-dimensional two-disk system.
% The radii of the two disks can be changed.
%
%%%%%%%%%%%%%%%%%%%%%%%%%%%%%%%%%%%%%%%%%%%%%%%%%%%%%%%%%%%%%%%%%%%%%%%%

clear all;
close all;

ArrayOfCircles=1;

nu= 750 * 100.0;      % The wavenumber (cm-1) * 100)
phi=pi/2.0;
k=2*pi*nu;
kx=k*cos(phi);
ky=k*sin(phi);
clear phi;

NCx=1; %do not change
NCy=2; %do not change

r1 = 10^-5;      % Disk no 1
r2 = 0.5*r1;    % Disk no 2

R=max(r1,r2);
Nx=50;          % Resolution in x-direction
Ny=100;        % Resolution in y-direction
N=Nx*Ny;
a=2*NCx*R;
b=2*NCy*R;
n_index=1.7;   % Refractive index of the disk(s)

dx=a/Nx; % spacing in x-direction
dy=b/Ny; % spacing in y-direction

x=zeros(1,N);
y=zeros(1,N);
for i=1:Nx
    for l=1:Ny

        j=(l-1)*Nx+i;
        x(j)=(i-0.5)*dx;
        y(j)=(l-0.5)*dy;

    end
end

G=zeros(N,N);

for j=1:N
    for m=1:N

```



```

% H is not defined for zero argument
if (j==m)
    G(j,m)=0.0;
else
    Z=k*sqrt((x(j)-x(m))*(x(j)-x(m))+(y(j)-y(m))*(y(j)-y(m)));
    G(j,m)=besselh(0,Z); %besselh(nu,Z) gives Hankel function
                        H_0^+
end

end

end

% Establish the potential
v=zeros(1,N);
for m=1:N

    x1circle=r1;
    y1circle=r1;

    x2circle=r1;
    y2circle=r1*2+r2;

    rn1=sqrt((x(m)-x1circle)*(x(m)-x1circle)+(y(m)-y1circle)*(y(m)-
y1circle));
    rn2=sqrt((x(m)-x2circle)*(x(m)-x2circle)+(y(m)-y2circle)*(y(m)-
y2circle));

    if (rn1<r1)
        v(m)=1.0-n_index*n_index;

    elseif (rn2<r2)
        v(m)=1.0-n_index*n_index;
    end

end

end

%plots the potential
v_reshaped=reshape(v,Nx,Ny);
figure;
pcolor(v_reshaped');
set(gcf,'Color',[1 1 1]);

%vMat=reshape(v,Nx,Ny);
Gtilde=zeros(N,N);

for j=1:N
    for m=1:N

        Gtilde(j,m)=G(j,m)*v(m);

    end

end
end

```

```

clear G;
clear v;

eikr=zeros(1,N);
for j=1:N
    eikr(j)=exp(1i*(kx*x(j)+ky*y(j)));
end
clear x y;

M=zeros(N,N);
IdentityMat=eye(N,N);
M=IdentityMat+1i*(k*k*dx*dy*0.25)*Gtilde;

clear Gtilde;
clear IdentityMat;

%% Solve Linear Equation by Matlab routine
psi_complex = linsolve(M,eikr');
psi_complex_reshaped=reshape(psi_complex,Nx,Ny);

Xplot=abs(psi_complex_reshaped).*abs(psi_complex_reshaped);

figure;
pcolor(Xplot');
set(gcf,'Color',[1 1 1]);

phi=zeros(Nx,Ny);
phi=angle(psi_complex_reshaped); % gives angles in the range -pi:pi

figure;
pcolor(phi');
set(gcf,'Color',[1 1 1]);

% Integrating over the absolute square of the wave function
linearIndexXplot=sub2ind(size(Xplot),Nx,Ny);
IntegralPsi=sum(Xplot(1:linearIndexXplot));

```




Norwegian University
of Life Sciences

Postboks 5003
NO-1432 Ås, Norway
+47 67 23 00 00
www.nmbu.no